

Pro-Apoptotic and Immunostimulatory Tetrahydroxanthone Dimers from the Endophytic Fungus *Phomopsis longicolla*

David Rönsberg,[†] Abdessamad Debbab,[†] Attila Mándi,[‡] Vera Vasylyeva,[§] Philip Böhler,^{||} Björn Stork,^{||} Laura Engelke,[⊥] Alexandra Hamacher,[⊥] Richard Sawadogo,[#] Marc Diederich,[#] Victor Wray,[∇] WenHan Lin,[○] Matthias U. Kassack,[⊥] Christoph Janiak,[§] Stefanie Scheu,[◆] Sebastian Wesselborg,^{||} Tibor Kurtán,[‡] Amal H. Aly,^{*,†} and Peter Proksch^{*,†}

[†]Institut für Pharmazeutische Biologie und Biotechnologie, Heinrich-Heine-Universität, Universitätsstrasse 1, 40225 Düsseldorf, Germany

[‡]Department of Organic Chemistry, University of Debrecen, POB 20, 4010 Debrecen, Hungary

[§]Institut für Anorganische Chemie und Strukturchemie, Heinrich-Heine-Universität, Universitätsstrasse 1, 40225 Düsseldorf, Germany

^{||}Institut für Molekulare Medizin, Universitätsklinikum Düsseldorf, Heinrich-Heine-Universität, Universitätsstrasse 1, 40225 Düsseldorf, Germany

[⊥]Institut für Pharmazeutische und Medizinische Chemie, Heinrich-Heine-Universität, Universitätsstrasse 1, 40225 Düsseldorf, Germany

[#]Laboratory of Molecular and Cellular Biology of Cancer (LBMCC), Hôpital Kirchberg, 9 rue Edward Steichen, 2540 Luxembourg, Luxembourg

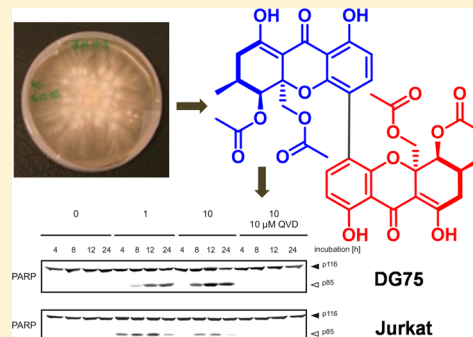
[∇]Helmholtz Centre for Infection Research, Inhoffenstraße 7, 38124 Braunschweig, Germany

[○]National Research Laboratories of Natural and Biomimetic Drugs, Peking University, Health Science Center, 100083 Beijing, China

[◆]Institut für Medizinische Mikrobiologie und Krankenhaushygiene, Heinrich-Heine-Universität, Universitätsstrasse 1, 40225 Düsseldorf, Germany

Supporting Information

ABSTRACT: Four tetrahydroxanthone dimers (1–4) and four biogenetically related monomers (5–8), including the new derivatives 4–6, were isolated from the endophyte *Phomopsis longicolla*. The absolute configurations of 2–4 were established for the first time by TDDFT electronic circular dichroism calculations, and that of phomoxanthone A (1) was revised by X-ray crystallography. Phomoxanthone A (1) showed the strongest pro-apoptotic activity when tested against a panel of human cancer cell lines, including cisplatin-resistant cells, whereas it was up to 100-fold less active against healthy blood cells. It was also the most potent activator of murine T lymphocytes, NK cells, and macrophages, suggesting an activation of the immune system in parallel to its pro-apoptotic activity. This dual effect in combating cancer cells could help in fighting resistance during chemotherapy. Preliminary structure–activity studies of isolated compounds and derivatives obtained by semisynthesis (9a–11) hinted at the location of the biaryl axis and the presence of acetyl groups as important structural elements for the biological activity of the studied tetrahydroxanthones.



INTRODUCTION

Cancer still poses one of the most serious health problems and ranks as the second leading cause of death in the Western World after heart/circulatory problems.¹ Problems in treating cancer are closely linked to chemoresistance against currently available cytostatic drugs.² During the onset of a chemotherapeutic cycle, cancer cells usually react favorably to the drugs administered, and a vast majority of the cancer cells are killed. A few surviving cells might display a highly chemoresistant phenotype due to successive mutations of oncogenes

and suppressor genes that deregulate the cell cycle.³ This type of chemoresistance is known as secondary or acquired resistance.⁴ Chemoresistance may also pre-exist in a few cells, which are then selected by chemotherapy.³ This model supports the idea of a heterogeneous population of cancer cells (intrinsic resistance).⁴ Resistant cancer cells are difficult to treat by currently available chemotherapy or by radiotherapy.

Received: September 17, 2013

Published: December 2, 2013

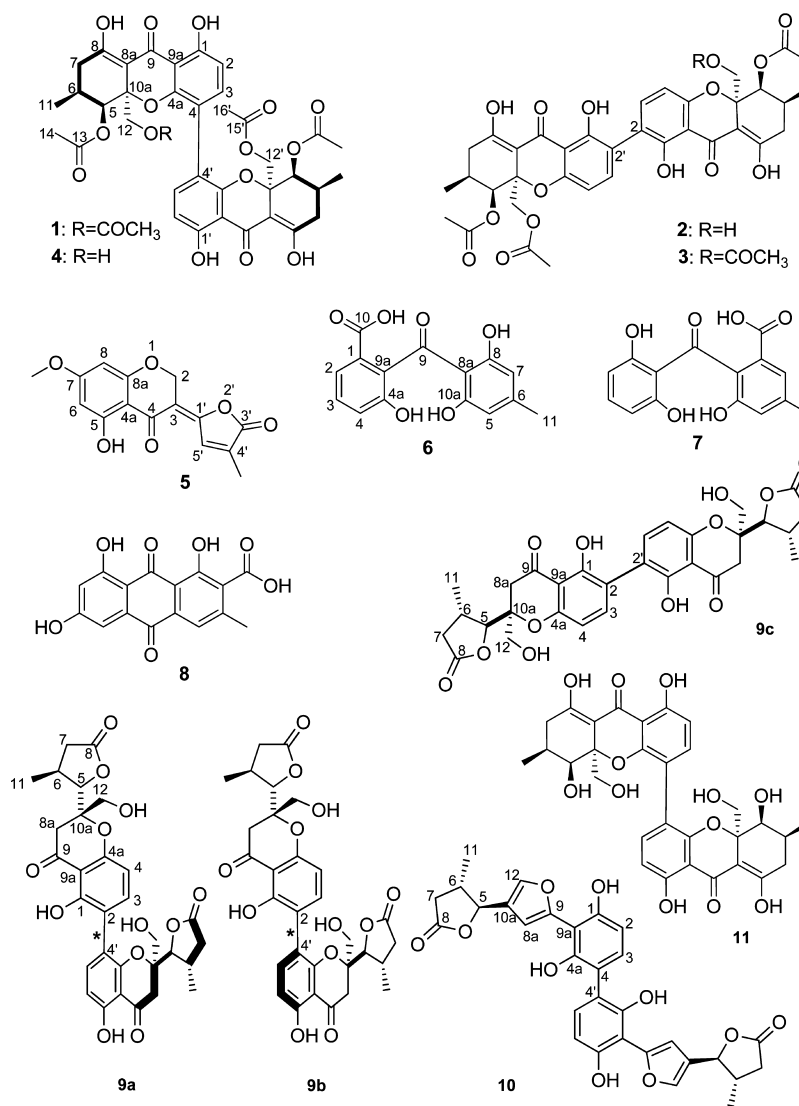


Figure 1. Chemical structures of compounds 1–11. The axial chiralities (*) of the atropodiastereomers (9a and 9b) have not been assigned.

They rapidly spread and develop metastases that attack vital organs of the body, with ultimate patient death. In this context, the identification of tumor-specific antigens and their recognition by T cells⁵ indicates the paradoxical fact that in spite of the natural capability of the immune system to recognize cancer cells, it often fails to control malignant growth. This may be explained by generalized immunodeficiency associated with tumor growth or by immunomodulatory properties of cancer within its microenvironment.⁶ The latter could be reversed by immunotherapy through activation of immune effector functions to promote tumor destruction.⁷ However, the impact of tumor immunology on the clinical management of cancer is still a matter of intensive investigation. Increasing evidence suggests that anticancer immune responses may contribute to the control of cancer after conventional therapy, helping to eliminate residual cancer cells or prevent micrometastases.⁸ Thus, the involvement of antitumor immune responses in the therapeutic management of cancer or the development of chemotherapeutic agents inducing specific immune responses, in addition to their direct cytotoxic effects on tumor cells, would attribute promising dual functions to a single molecule, offering a great improvement of cancer

treatment that is less hampered by or even able to prevent the development of chemical resistance.⁹

Natural products and natural product analogues have a long and impressive success story with regard to the treatment of cancer. More than two-thirds of the currently available anticancer drugs are derived from or inspired by nature.¹⁰ Prominent examples include plant-derived compounds such as paclitaxel; dimeric alkaloids from *Catharanthus roseus* (and their semisynthetic products); the camptothecin-derived drugs irinotecan and topotecan; and etoposide, a derivative of the naturally occurring lignan podophyllotoxin. However, recent research endeavors have shown that other less investigated organisms such as marine invertebrates and endophytic fungi harbor a wealth of structurally unprecedented and pharmacologically highly active compounds that can likewise provide important drug leads for the future.

Endophytic fungi spend the whole or part of their life cycle colonizing healthy tissues of their host plants, typically causing no apparent symptoms of disease.¹¹ This colonization is believed to contribute to host plant adaptation to biotic and abiotic stress factors,^{12–15} which in many cases has been correlated with fungal natural products. For instance, a vast array of antiproliferative secondary metabolites from endo-

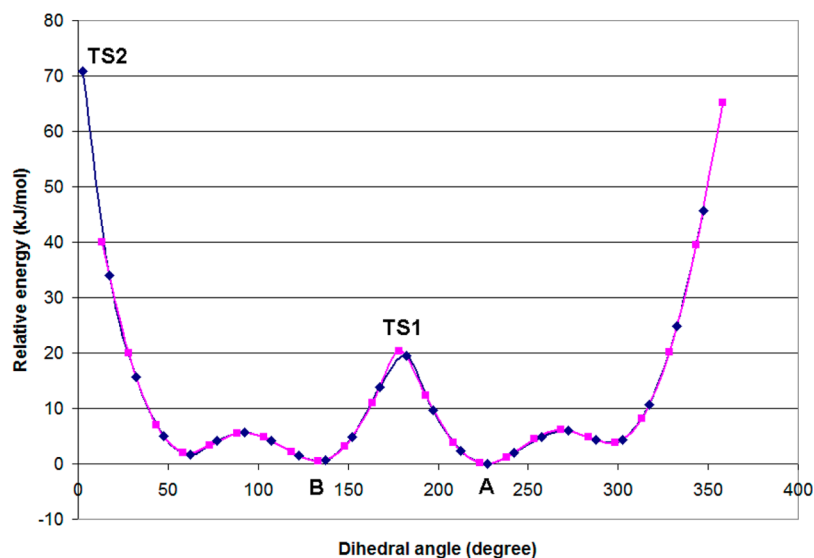


Figure 2. Preliminary torsional angle scans for determining the rotational energy barrier around the C2–C2' bond ($\omega_{C1'-C2'-C2-C1}$ torsional angle) of (5*R*,6*R*,10*aR*,5'*R*,6'*R*,10*a'**R*)-**2**. The scans were started from the lowest-energy in vacuo conformers of *M* and *P* helicity (A and B, respectively). Relative energy (kJ mol^{-1}) is plotted as a function of the $\omega_{C1'-C2'-C2-C1}$ torsional angle. TS1 and TS2 denote the two transition states for inversion of the helicity.

phytic fungi have hitherto been reported.¹⁶ Examples include the farnesyl protein transferase-inhibiting chaetomelic acids A and B isolated from endophytic *Chaetomella acutisea*,¹⁷ proapoptotic and c-Myc down-regulating secalonic acid D from the mangrove endophytic fungus ZSU44,¹⁸ heat shock protein (HSP90)-inhibiting radicicol from *Chaetomium chiversii*,¹⁹ and DNA polymerase inhibiting kasanosins A and B from *Talaromyces* sp.²⁰

It has been hypothesized that endophytes that survive under harsh environmental conditions should be prioritized for bioprospecting,^{10,21,22} as stress factors are known to induce biosynthetic pathways leading to bioactive metabolites. Mangrove swamps, with their high salinity and periodic changes in tidal submergence, represent one of the most stressful habitats for host plants and endophytes alike. Hence, endophytes from mangrove plants have recently attracted considerable attention from natural products chemists looking for new inspirations from nature.^{23–27} The present study focuses on the endophytic fungus *Phomopsis longicolla*, which was isolated from leaves of the mangrove plant *Sonneratia caseolaris* growing in South China. The genus *Phomopsis* contains more than 900 species that occur in a wide range of habitats, and some of them are known as endophytes.²⁸ Endophytic species of *Phomopsis* are known to produce an impressive variety of bioactive natural products,^{29–41} including the tremorgenic mycotoxins paspalitrems A and C; the actin-binding cytochalasins,⁴² which are potent inhibitors of microtubule assembly; and xanthone derivatives such as phomoxanthone A (**1**) (Figure 1).^{17,26–29} Our interest in *P. longicolla* was aroused by the strong inhibitory activity of a crude EtOAc extract (dose: 10 $\mu\text{g/mL}$) of the endophyte in an MTT assay using the mouse lymphoma cell line L5178Y (data not shown). Subsequent chromatographic separation of the extract yielded eight natural products, including the new 12-deacetylphomoxanthone A (**4**), phomo-2,3-dihydrochromone (**5**), and isomonodictyphenone (**6**) (Figure 1) in addition to **1**, whereas dicerandrols B (**2**) and C (**3**), monodictyphenone (**7**), and endocrocins (**8**) have been described previously. In addition, five semisynthetic derivatives (**9a–11**; Figure 1)

were obtained following acidic or alkaline hydrolysis of **1**. All of the compounds were unequivocally identified on the basis of a combination of multidimensional NMR and MS data and comparison with the literature. The absolute configuration of **1** was revised by X-ray crystallography compared with the originally reported configuration,⁴³ and those of **2–4** were established for the first time by CD calculations and comparison with **1**. The dimeric tetrahydroxanthone derivatives **1–4** showed strong inhibition of proliferation of the lymphoma cell line L5178Y, with phomoxanthone A (**1**) as the most active compound. Interestingly, the activity of phomoxanthone A extended also to several other human cancer cell lines, including cancer cells that are resistant to the well-known chemotherapeutic drug cisplatin, making this compound an interesting candidate for further studies. The cytotoxicity of **1** displayed selectivity toward cancer cells, as it was found to be over 100-fold less toxic to healthy blood cells than to lymphoma cell lines. We could also show for the first time that the cytostatic activity of **1** is due to its pro-apoptotic potential. Phomoxanthone A (**1**) followed by the less active dicerandrols B (**2**) and C (**3**) furthermore showed clear upregulation of murine CD69⁺ T and NK cells as well as of macrophages, indicating that **1** exhibits a dual efficacy in combating cancer cells through induction of apoptosis and activation of the immune system, which could help in fighting tumor resistance during chemotherapy.

RESULTS AND DISCUSSION

The EtOAc extract of *Phomopsis longicolla*, following cultivation on rice solid medium, was subjected to column chromatography using silica gel, Diaion HP20, and Sephadex LH-20 as alternating stationary phases followed by semipreparative HPLC for final purification. The tetrahydroxanthone dimer phomoxanthone A (**1**) (Figure 1) was obtained as the major constituent upon fractionation of the crude extract. Compound **1** had been reported previously to have the (a*S*,*S**R*,6-*R*,10*aR*,5'*R*,6'*R*,10*a'**R*) configuration,^{43,44} which was revised in this study. In addition, the known tetrahydroxanthone dimers dicerandrols B (**2**)⁴⁵ and C (**3**)⁴⁵ (Figure 1) were readily

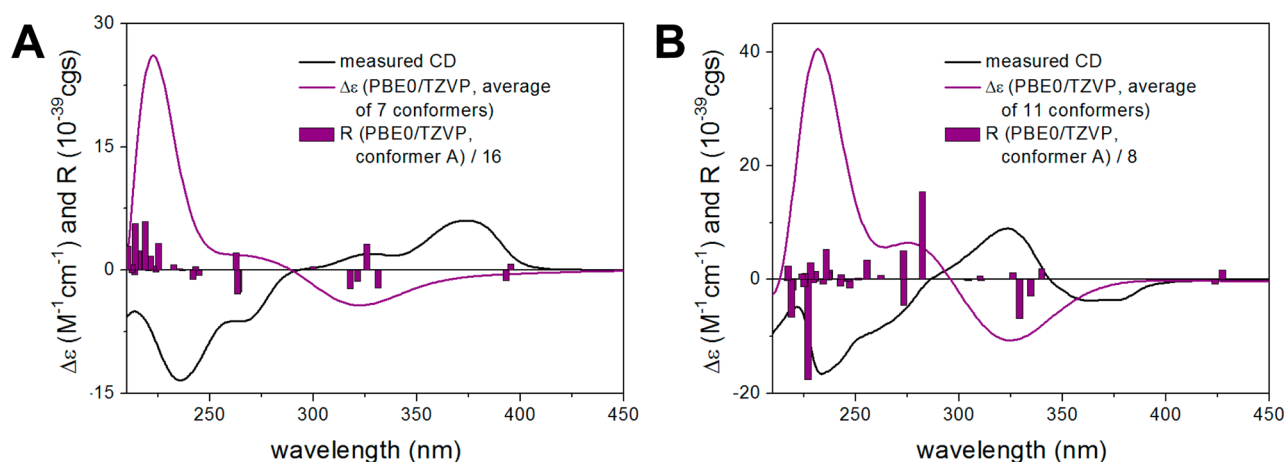


Figure 3. Experimental and PBE0/TZVP-calculated ECD spectra of the B3LYP/TZVP- and B3LYP/6-31G(d)-reoptimized low-energy geometries of (A) (5*R*,6*R*,10*aR*,5'*R*,6'*R*,10*a'R*)-**2** and (B) (5*R*,6*R*,10*aR*,5'*R*,6'*R*,10*a'R*)-**3**, respectively, in acetonitrile. Bars represent the calculated rotational strengths of the lowest-energy conformers.

identified by detailed analyses of their mass spectra and 1D and 2D NMR spectra as well as by comparison with published data.

For **2** and **3**, only the relative configuration had been published previously. Their absolute configurations were determined in the present work by TDDFT electronic circular dichroism (ECD) calculations. Dicerandrol B (**2**) features a 2,2'-linkage of two slightly different homochiral monomeric units, which in analogy to secalonic acid **F**⁴⁶ is expected to allow interconversion of the *P* and *M* helicity forms at room temperature, since the 1- and 1'-OH groups at the *ortho* positions do not impose sufficient steric hindrance to interrupt free rotation about the biaryl axis. In order to exclude the possibility of axially chiral atropisomers and to estimate the rotational barrier around the C2–C2' bond, torsional scans were performed on the $\omega_{C1'-C2'-C2-C1}$ angle from the lowest-energy conformers of *P* and *M* helicity in vacuo (Figure 2). The scans started from the two low-energy conformers (A and B in Figure 2) and gave approximately the same results, showing two energy barriers with different energies. Next, transition-state calculations were run at the two maxima, which identified the energy barrier of the lower transition state (TS1) as 20.5 kJ/mol and that of the higher one (TS2) as 70.9 kJ/mol (Figure S1 in the Supporting Information). The 20.5 kJ/mol energy barrier indicated that the *P* and *M* helicity forms can freely equilibrate at room temperature, and they appear as conformers with different populations. The *P* and *M* helicity conformers are expected to produce different ECD curves, and hence, their populations determine the experimental solution ECD spectrum. The populations of the *P* and *M* helicity conformers are governed by the central chirality elements, and their accurate estimation by conformational analysis is crucial for the agreement of the computed and experimental ECD spectra.

Dicerandrol B (**2**) showed a broad positive Cotton effect (CE) at 373 nm with shoulders at 344 and 328 nm, and three negative CEs at 268, 233, and 198 nm. The solution TDDFT ECD approach was pursued to determine the absolute configuration of **2**. The initial MMFF conformational search of the arbitrarily chosen (5*R*,6*R*,10*aR*,5'*R*,6'*R*,10*a'R*)-**2** resulted in 84 conformers in a 21 kJ/mol energy window, DFT reoptimization of which yielded 11, 7, and 11 conformers at the B3LYP/6-31G(d) level in vacuo, the B3LYP/TZVP level with the PCM model for acetonitrile, and the M06/TZVP level⁴⁷

with the PCM model for MeCN, respectively. The three methods of conformational analysis applied for the optimizations yielded similar sets of conformers with a predominant population of the *M* helicity conformers (negative $\omega_{C1'-C2'-C2-C1}$ torsional angle). For instance, the B3LYP/TZVP reoptimization with the PCM model for acetonitrile resulted in seven conformers above 2% population (Figure S2 in the Supporting Information). The lowest-energy conformer had *M* helicity with $\omega_{C1'-C2'-C2-C1} = -122.3^\circ$ and 30.8% population, and conformers C–F also had *M* helicity with slightly different orientations of the acetoxy groups. Conformer B had *P* helicity with $\omega_{C1'-C2'-C2-C1} = +124.75^\circ$ and 21.8% population, and conformer G (2.0%) had also *P* helicity. The overall population of the *M* helicity conformers was 56.6%, while that of the *P* helicity conformers was 23.8%. The C5 and C10a (C5' and C10a') substituents are trans-diaxial in all conformers, and the C6 (C6') methyl group adopts an equatorial orientation. The Boltzmann-averaged ECD spectra were calculated with the TZVP basis set and three functionals (B3LYP, BHandHLYP, and PBE0) for the three sets of solution conformers of (5*R*,6*R*,10*aR*,5'*R*,6'*R*,10*a'R*)-**2**. The *M* and *P* helicity conformers had opposite CEs for the two high-energy transitions, but all of the conformers had a negative CE around 330 nm. The Boltzmann-averaged ECD spectra were near mirror images of the experimental spectrum (Figure 3A), which allowed the determination of the absolute configuration as (5*S*,6*S*,10*aS*,5'*S*,6'*S*,10*a'S*).

Dicerandrol C (**3**) is a homodimer and the acetoxy derivative of dicerandrol B (**2**), but interestingly, it has negative CEs at 373 and 365 nm, opposite to those of **2**. In order to identify the origin of their different ECDs, TDDFT calculations were performed. The MMFF conformational search of (5*R*,6*R*,10*aR*,5'*R*,6'*R*,10*a'R*)-**3** resulted in 71 conformers in a 21 kJ/mol energy window, DFT reoptimization of which yielded 11 and 17 conformers at the B3LYP/6-31G(d) level in vacuo and the M06/TZVP level with the PCM model for MeCN, respectively (Figure S3 in the Supporting Information). Both the gas-phase and PCM-model ECD calculations showed nearly mirror-image spectra compared with the experimental one, but the lowest-energy negative transition could not be predicted well in the averaged spectra. However, the ECD spectra of the lowest-energy conformers obtained at both levels showed positive computed CEs above 340 nm, giving further

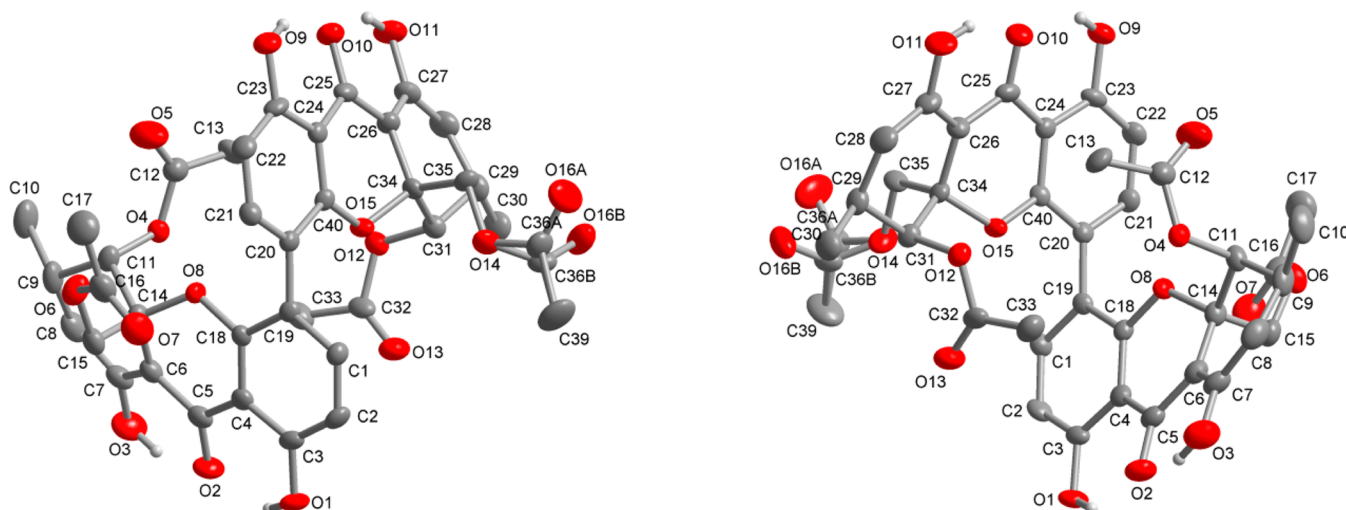


Figure 4. Two views of the molecular structure of phomoxanthone A (**1**) (50% thermal ellipsoids) with the determined absolute configuration. For clarity, H atoms on carbons are not shown. The torsional disorder of one acetyl group should be noted.

support to the mirror-image relationship of the calculated and measured ECD spectra. This finding also suggests that the population of the lowest-energy conformers may have been underestimated at both levels of theory. The lowest-energy conformer of the M06/TZVP reoptimization with the PCM model had *P* helicity with $\omega_{C1'-C2'-C2-C1} = +61.3^\circ$, and in the B3LYP/6-31G(d) in vacuo optimization, the lowest-energy conformer had *P* helicity with $\omega_{C1'-C2'-C2-C1} = +132.1^\circ$. The overall population of the *P* helicity conformers totaled 47.3%, while that of the *M* helicity ones was 29.9%. The additional acetoxy group changed the preferred sign and value of the biaryl dihedral angle, and this conformational change is responsible for the different ECD spectra of **2** and **3**. (*5R,6R,10aR,5'R,6'R,10a'R*)-**3** produced near mirror-image Boltzmann-averaged ECD spectra compared with the experimental one at the three levels of ECD calculations, which allowed the assignment of the absolute configuration as (*5S,6S,10aS,5'S,6'S,10a'S*) (Figure 3B).

The all-*S* absolute configurations of dicerandrols **B** and **C** prompted us to reinvestigate the absolute configuration of phomoxanthone A (**1**).⁴³ Since our phomoxanthone A sample was isolated together with dicerandrols **B** and **C**, it was expected also to contain monomers with the all-*S* absolute configuration on the basis of biogenetic considerations. Our phomoxanthone A sample showed the same specific rotation and ECD data as the previously reported one, for which the (*aS,5R,6R,10aR,5'R,6'R,10a'R*) absolute configuration had been assigned.⁴³ Theoretically, it was possible that the phomoxanthone A sample isolated in this study could have the (*aS,5S,6S,10aS,5'S,6'S,10a'S*) absolute configuration, since the chiroptical parameters are determined by the axial chirality. In order to clarify this issue, an X-ray analysis of our phomoxanthone A sample was initiated.

In the previous study⁴³ phomoxanthone A (**1**) crystals were obtained as yellowish needles from a dichloromethane/diethyl ether solution. It was reported that **1** crystallized in space group *P*₂₁ with two independent but geometrically identical molecules per asymmetric unit as well as two solvent water molecules. X-ray analysis of these crystals revealed only the relative configuration of the stereogenic elements, whereas the absolute configuration of the compound was deduced on the basis of semiempirical ECD calculations on the solid-state con-

formers.⁴³ The authors noted that “in the absence of significant anomalous scattering effects, the Flack parameter is essentially meaningless. Accordingly, Friedel pairs were merged.”

In the present study, **1** also crystallized in the non-centrosymmetric space group *P*₂₁ from EtOAc solution but with only one phomoxanthone A molecule in the asymmetric unit (Figure 4 and Figure S4 in the Supporting Information) and one water and one EtOAc solvent molecule in the unit cell.

We could now determine the absolute structure from anomalous dispersion with Cu-*K* α radiation using the Flack parameter (for details, see the Supporting Information).^{48–51} Friedel pairs were not merged. The absolute configuration of phomoxanthone A (**1**) was determined as (*aR,5S,6S,10aS,5'S,6'S,10a'S*), which is enantiomeric to the previously reported absolute configuration (Figure 1 and Figure S5 in the Supporting Information). Accordingly, the previously reported absolute configuration of **1** has to be revised. In order to reveal the origin of the previous wrong configurational assignment on the basis of ECD calculations, TDDFT ECD calculations were performed on the previously reported and the recently determined X-ray structures of **1** at three levels of theory (B3LYP/TZVP, BHandHLYP/TZVP, and PBE0/TZVP). Since the previous assignment was made on the basis of a semiempirical ECD method, ECD spectra of the B3LYP/6-31G(d)-optimized and original X-ray structures of **1** were also calculated by the semiempirical ZINDO method for comparison. All of the DFT methods applied to the optimized and original X-ray geometries of (*aS,5R,6R,10aR,5'R,6'R,10a'R*)-**1** gave opposite effects relative to the negative CE at 341 nm and the positive CE at 316 nm in the solution ECD spectrum as well as to the intense negative CEs at 228 and 222 nm when they were red-shifted by 12 nm (Figure 5).

In contrast, the agreement with the solid-state ECD spectrum was poor, and the computed low-energy negative transition had no oppositely signed counterpart in the experimental solid-state ECD spectrum (Figure S6 in the Supporting Information). The negative CE at 342 nm in the solution ECD spectrum disappeared in the solid-state ECD spectrum, most likely as a result of intermolecular exciton-coupled interactions in the solid state. The computed ZINDO spectra showed poor agreement with the experimental spectrum compared with those from the DFT methods, and

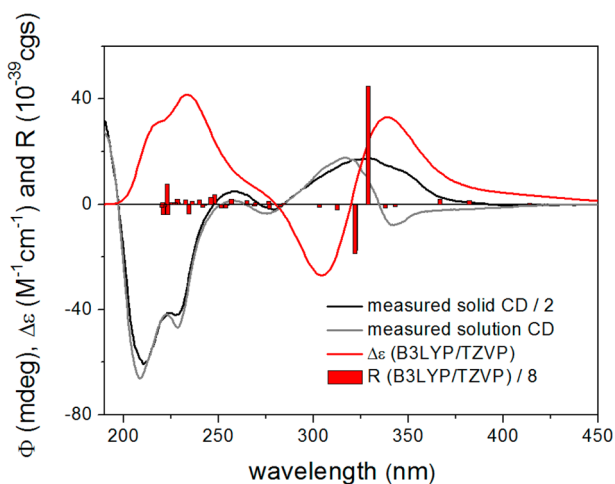


Figure 5. Experimental and B3LYP/TZVP-calculated ECD spectra of the X-ray conformers of (aS,5R,6R,10aR,5'R,6'R,10a'R)-**1** in vacuo (average of the two conformers). The computed spectrum is shifted 12 nm to the red.

the spectra had to be shifted by about 100 nm. The intermolecular interactions in the solid state and the missing negative band of the solid-state ECD spectrum could have led to the wrong configurational assignment of phomoxanthone A during the previously published configurational assignment by ECD calculations. It has to be noted as well that even a comparison of the DFT-computed ECD spectra of the X-ray geometry with the solid-state experimental spectrum would not allow an unambiguous conclusion.

The new compound **4** has the molecular formula $C_{36}H_{36}O_{15}$ as determined by HR-ESI-MS (m/z 709.2127 [$M + H$] $^+$), showing a mass difference of 42 amu relative to **1**, which corresponds to the absence of an acetyl moiety. In addition, the UV spectra of **4** were almost identical to those of **1**, indicating that the two compounds share very similar structural scaffolds. The 1H NMR spectrum of **4** exhibited a set of signals similar to those observed for **1** but with only three acetyl methyl groups resonating at δ_H 1.75 (16'-CH₃), 2.10 (14-CH₃), and 2.11 (14'-CH₃) (Table 1). The ^{13}C NMR and DEPT spectra revealed the presence of 36 carbon atoms in total, including signals for only five carbonyl groups (Table 1). The structure was further confirmed by thorough analysis of 2D NMR spectra (Figure 6). The position of the acetyl functions was realized from 3J correlations of H5/H5' to C13/C13' and of (H12')₂ to C15', thus indicating the loss of the acetyl function present at 12-OH in **1**. Furthermore, ROESY correlations among H5/H5', H6/H6', and (H12)₂/(H12')₂ indicated their cofacial orientation. Analysis of coupling constants indicated that H6 ($J_{6,7\beta} = 10$ Hz) and H5 ($J_{5,6} = 1.7$ Hz) are in axial and equatorial positions, respectively. Compound **4** was thus identified as the new natural product 12-deacetylphomoxanthone A (Figure 1). The ECD spectrum of **4** was found to be quite different from that of phomoxanthone A (**1**) above 240 nm. A broad positive CE at 346 nm and weak negative plateau between 274 and 310 nm were observed for **4** instead of the negative CE at 341 nm and the positive CE at 316 nm for **1**. These differences are attributed to the lack of the acetoxy group, which changes the preferred biaryl dihedral angle as demonstrated by dicerandrols B and C.

HR-ESI-MS analysis of the new compound **5** showed the molecular ion peak at m/z 289.0707 [$M + H$] $^+$, indicating the

molecular formula $C_{15}H_{12}O_6$. The 1H NMR spectrum (Table 2) exhibited two aromatic *meta*-coupled protons at δ_H 6.88 (H6) and 6.73 (H8), one olefinic proton singlet at δ_H 6.27 (HS'), one aliphatic oxygenated methylene group at δ_H 5.15 [(H2)₂], one methyl group at δ_H 2.38 (4'-CH₃), and one methoxy group at δ_H 3.91 (7-OCH₃). The ^{13}C NMR spectrum (Table 2) displayed 15 carbon atoms, including a keto group, an ester carbonyl group, 10 olefinic carbon signals (including four oxygenated carbons), one oxygenated methylene, one methoxy group, and one methyl group. The COSY spectrum revealed the *meta*-coupled protons H6 and H8 as well as a long-range coupling between 4'-CH₃ and HS' (Figure 6). HMBC measurements (Figure 6) confirmed the presence of a chromone moiety from the observed correlations of H8 to C4a, C6, C7, and C8a; H6 to C4a, C5, C7, and C8; and (H2)₂ to C1', C4, C4a, and C8a. The oxofuranylidene moiety was deduced from the correlations of HS' to C2, C3, C4, C3', and 4'-CH₃ and 4'-CH₃ to C3' and C5'. The position of the methoxy group was confirmed by its correlation to C7. Furthermore, analysis of the ROESY spectrum allowed the assignment of the stereochemistry around the C3=C1' double bond. The absence of a cross-peak between (H2)₂ and HS' indicated spatial separation of these protons and thus an *E* configuration of the double bond in **5**, for which we suggest the name phomo-2,3-dihydrochromone (Figure 1).

Compounds **6** and **7** shared the same molecular formula of $C_{15}H_{12}O_6$, as indicated by their HR-ESI-MS data (m/z 289.07028 [$M + H$] $^+$). 1H and ^{13}C NMR, COSY, and HMBC data (Table 3 and Figure 6) indicated that **7** was identical and **6** was closely related to the known compound monodictyphenone.⁵² The HMBC correlations of 11-CH₃ to C5, C6, and C7 unambiguously showed that the methyl group is attached at C6 of the symmetric dihydroxyphenyl moiety in **6**, in contrast to **7**, where the methyl substituent is located at C3. This could be explained by cleavage of the presumed anthraquinone precursor emodin either between C4a and C10 or C10a and C10, resulting in **6** or **7**, respectively (Scheme 1). Accordingly, **6** was identified as a new natural product for which we suggest the name isomonodictyphenone (Figure 1).

In addition to the previously described natural products, the known compound endocrocin (**8**) was isolated and identified by comparison of its UV, NMR, and mass spectral data with published values.^{53,54}

The biosynthetic relationship between the secondary metabolites of polyketide origin, including monomeric and dimeric xanthone derivatives, has been the subject of intensive investigations.^{21,55–57} The polyketides isolated from *P. longicolla* in this study are assumed to be derived from a C_{16} -octaketide that undergoes condensation and cyclization to yield anthraquinone precursors such as endocrocin (**8**) or emodin, even though the latter was not isolated in this study. Emodin may be enzymatically transformed into monodictyphenone (**7**) by oxidative ring opening^{58–62} between C4a and C10. Isomonodictyphenone (**6**) most likely originates in the same way by cleavage of the covalent C10–C10a bond of emodin. Benzophenones can be enzymatically converted into xanthenes by oxidative phenolic coupling, which is followed by dimerization to yield phomoxanthenes, dicerandrols, and similar compounds, as proposed for secalonic acids by Kurobane et al.⁵⁷ Breinholt et al.⁶³ showed that the triketide xanthofusins emerges from an aromatic precursor by oxidative ring opening, which may explain the formation of the oxofuranylidene substructure in phomo-2,3-dihydrochromone

Table 1. ^1H and ^{13}C NMR, COSY, and HMBC Data for 4 at 600 (^1H) or 75 (^{13}C) MHz (MeOH- d_4 , δ in ppm, J in Hz)

atom	δ_{H}	δ_{C}	COSY	HMBC
1		162.5		
2	6.46, <i>d</i> (8.7)	110.3	3	1, 4, 4a, 9, 9a
3	7.41, <i>d</i> (8.7)	142.4	2	1, 4', 4a, 9a
4		116.8		
4a		155.3		
5	5.59, <i>d</i> (1.7)	72.5	6	6, 7, 8a, 10a, 11, 12, 13
6	2.49, <i>m</i>	29.1	5, 7, 11	7, 11
7	2.49, <i>dd</i> (6.2, 18.0)	34.1	6, 7, 11	5, 6, 8, 8a
	2.33, <i>dd</i> (10.0, 18.0)			6, 8, 8a, 11
8		178.8		
8a		102.0		
9		189.1		
9a		107.5		
10a		83.8		
11	1.00, <i>d</i> (6.4)	17.7	6, 7	5, 6, 7
12	3.87, <i>d</i> (13.2)	65.5	12	5
	3.53, <i>d</i> (13.2)			5, 8a, 10a
13		171.9		
14	2.10, <i>s</i>	20.7		13
1'		162.5		
2'	6.43, <i>d</i> (8.7)	109.6	3'	1', 4', 4a', 9', 9a'
3'	7.33, <i>d</i> (8.7)	142.0	2'	1', 4, 4a', 9a'
4'		116.8		
4a'		155.8		
5'	5.49, <i>br. s</i>	71.7	6'	6', 7', 8a', 10a', 11', 12', 13'
6'	2.49, <i>m</i>	28.8	5', 7', 11'	7', 11'
7'	2.54, <i>dd</i> (5.5, 17.5)	34.1	5', 6', 7', 11'	5', 6', 8', 8a'
	2.35, <i>dd</i> (10.0, 17.5)		5', 6', 7', 11'	6', 8', 8a', 11'
8'		179.4		
8a'		100.1		
9'		189.1		
9a'		107.6		
10a'		82.3		
11'	1.01, <i>d</i> (6.5)	17.7	6', 7'	5', 6', 7'
12'	4.78, <i>d</i> (12.9)	65.5	12'	5', 10a', 15'
	4.01, <i>d</i> (12.9)			5', 8a', 10a', 15'
13'		171.9		
14'	2.11, <i>s</i>	20.8		13'
15'		172.4		
16'	1.75, <i>s</i>	20.4		15'

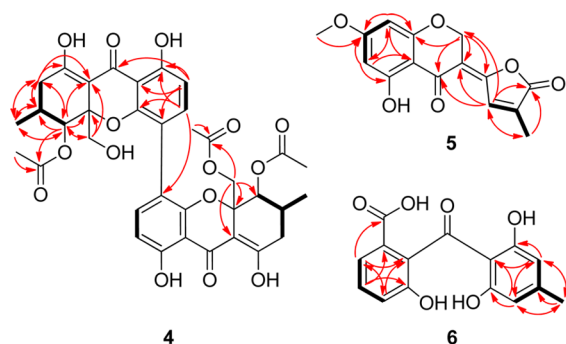


Figure 6. Key COSY (bold black bonds) and HMBC (red arrows) correlations in 4–6.

(5). Accordingly, a plausible biosynthetic pathway for the polyketides isolated in this study could be depicted as shown in Scheme 1.

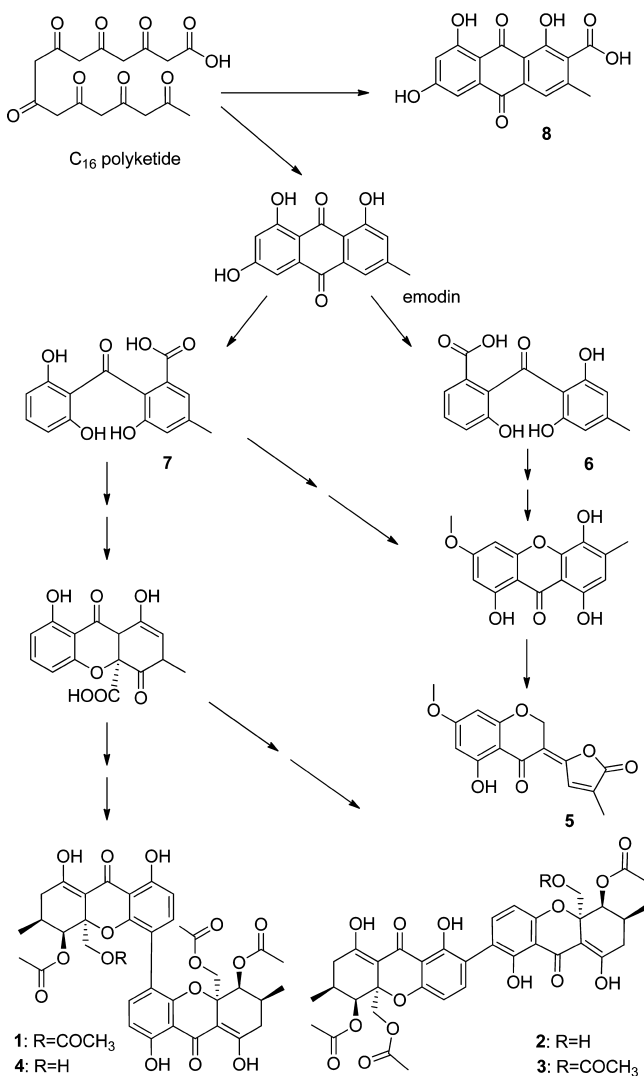
Table 2. ^1H and ^{13}C NMR, COSY, and HMBC Data for 5 at 300 (^1H) or 100 (^{13}C) MHz (MeOH- d_4 , δ in ppm, J in Hz)

atom	δ_{H}	δ_{C}	COSY	HMBC
2	5.15, <i>s</i>	63.6		1', 3, 4, 4a, 8a
3		113.3		
4		178.3		
4a		107.6		
5		172.0		
6	6.88, <i>d</i> (2.5)	111.2	8	4a, 5, 7, 8
7		165.2		
8	6.73, <i>d</i> (2.4)	104.3	6, 7-OCH ₃	4a, 6, 7, 8a
8a		161.3		
1'		157.5		
3'		167.7		
4'		114.3		
5'	6.27, <i>s</i>	114.3	4'-CH ₃	2, 3, 4, 3', 4'-CH ₃
7-OCH ₃	3.91, <i>s</i>	56.5	8	7
4'-CH ₃	2.38, <i>s</i>	19.2	5'	3', 5'

Table 3. ^1H and ^{13}C NMR, COSY, and HMBC Data for **6** at 600 (^1H) or 100 (^{13}C) MHz ($\text{MeOH}-d_4$, δ in ppm, J in Hz)

atom	δ_{H}	δ_{C}	COSY	HMBC
1		130.0 ^a		
2	7.53, <i>dd</i> (1.0, 7.9)	122.0	3, 4	4, 9a, 10
3	7.28, <i>t</i> (7.9)	129.5	2, 4	1, 4a
4	7.05, <i>dd</i> (1.0, 7.9)	120.8	2, 3	2, 9a
4a		154.6		
5	6.16, ^b <i>s</i>	108.7 ^c	11	7, 8a, 10a, 11
6		149.0 ^a		
7	6.16, ^b <i>s</i>	108.7 ^c	11	5, 8, 8a, 11
8		163.4 ^d		
8a		110.1 ^a		
9		– ^e		
9a		135.0 ^a		
10		169.2		
10a		163.4 ^d		
11	2.24, <i>s</i>	21.5	5, 7	5, 6, 7

^aNo ^{13}C NMR signal was detected; the chemical shift was deduced from the HMBC correlation. ^{b,c,d}Superimposed signals due to chemical equivalence. ^eNo ^{13}C NMR signal was detected.

Scheme 1. Putative Biosynthetic Pathway for the Polyketides **1–8**

To increase the chemical diversity of congeners for a first evaluation of structure–activity relationships, the dominant natural product phomoxanthone **1** was subjected to acidic and alkaline hydrolysis. Acidic hydrolysis according to the method described by Isaka et al.⁴⁴ resulted in the formation of **11**, a previously described deacetyl analogue of **1**. On the other hand, alkaline hydrolysis of **1** with alcoholic NaOH at room temperature yielded the new derivatives **9a–c**, whereas treatment of **1** with aqueous NaOH under reflux resulted in the formation of a single new derivative (**10**). By analogy with **11**, **9a–c** showed a difference of 168 amu relative to **1** upon mass spectral analysis, corresponding to the loss of four acetate functions. However, inspection of the NMR data indicated further structural rearrangements in the core structures of **9a–c**.

The molecular formula of **9a** was assigned as C₃₀H₃₀O₁₂ on the basis of HR-ESI-MS data showing the molecular ion peak at m/z 583.18110 [M + H]⁺. The ^1H NMR spectrum (Table 4) revealed two almost identical sets of signals, indicating an asymmetrical dimeric structure composed of closely related monomers. It exhibited two aromatic and two aliphatic hydroxy groups resonating at δ_{H} 12.01 (1-OH), 11.74 (1'-OH), 5.45 (12'-OH), and 5.35 (12-OH). Signals of the aromatic protons appeared at δ_{H} 7.37 (H3'), 7.34 (H3), 6.50 (H2'), and 6.44 (H4), thus indicating two sets of *ortho*-coupled protons, as found in the biaryl units of other phomoxanthone derivatives.⁴⁴ In total, six methylene groups were detected at δ_{H} 3.75/3.66 [(H12')₂], 3.66 [(H12)₂], 3.18/2.83 [(H8a)₂], 3.10/3.06 [(H8a')₂], 2.78/2.20 [(H7')₂], and 2.25/1.93 [(H7)₂]. The remaining signals were assigned to two oxymethine protons at δ_{H} 4.39 (H5') and 4.21 (H5), two tertiary methine groups at δ_{H} 2.87 (H6') and 2.72 (H6), and two methyl groups at δ_{H} 1.15 (11'-CH₃) and 1.02 (11-CH₃). Thorough analyses of HMBC spectral data (Table 4 and Figure 7) allowed the construction of two partially saturated γ -pyrone moieties annulated to the aromatic rings. The involved methylene groups (8a-CH₂/8a'-CH₂) showed correlations to the sp² carbons C9a/C9a', the carbonyl carbons C9/C9', and the sp³ carbons C10a/C10a'. According to the molecular formula, the unsaturation index of **9a** is 16. The presence of four carbonyl groups [δ_{C} 197.7 (C9'), 197.5 (C9), 175.9 (C8), and 175.7 (C8')] and the tetracyclic biaryl scaffold accounted for 14 elements of unsaturation, thus indicating that the remaining part of **9a** should include two aliphatic ring systems. The structures of the latter were established by exhaustive analyses of the 2D NMR spectral data (Figure 7). Correlations of the tertiary methine protons H6/H6' to the oxymethines H5/H5', the methylene groups 7-CH₂/7'-CH₂, and the methyl groups 11-CH₃/11'-CH₃ were observed in the COSY spectrum, thus establishing the fragments 5-CH-6-CH(11-CH₃)-7-CH₂ and 5'-CH-6'-CH(11'-CH₃)-7'-CH₂. Moreover, the HMBC spectrum provided a full set of all possible ²*J* and ³*J* correlations for H5/H5', H6/H6', and (H7)₂/(H7')₂, confirming the fragment deduced from the COSY spectrum and allowing the construction of two 3-methyl- γ -butyrolactone moieties on the basis of the correlations observed from H5/H5' and (H7)₂/(H7')₂ to C8/C8'. The two 3-methyl- γ -butyrolactone rings were found to be linked to the tetracyclic biaryl skeleton at C10a and C10a', as indicated by the ³*J* correlations of the tertiary methine protons H5/H5' to C10a/C10a'. The 2,4'-linkage in the biaryl system was proven by HMBC correlations of H3 to C4'; H3' to C2; and 1-OH/1'-OH to C1/C1', C2/C2', and C9a/C9a'. The two oxymethine protons (H5/H5')

Table 4. ^1H and ^{13}C NMR, COSY, and HMBC Data for 9a–c at 600 (^1H) or 100 (^{13}C) MHz (DMSO- d_6 , δ in ppm, J in Hz)

atom	9a				9b				9c			
	δ_{H}	δ_{C}	COSY	HMBC	δ_{H}	δ_{C}	COSY	HMBC	δ_{H}	δ_{C}	COSY	HMBC
1		157.7				157.5				159.2		
2		116.1				116.4				115.6		
3	7.34, <i>d</i> (8.5)	139.5	4	1, 4', 4a	7.35, <i>d</i> (8.5)	139.8	4	1, 4', 4a	7.33, <i>d</i> (8.5)	136.2	4	1, 2', 4a
4	6.44, <i>d</i> (8.5)	106.8	3	2, 4a, 9, 9a	6.52, <i>d</i> (8.6)	106.7	3	2, 4a, 9, 9a	6.47, <i>d</i> (8.5)	105.6	3	2, 4a, 9a
4a		158.5				157.8				157.2		
5	4.21, <i>d</i> (3.6)	86.3	6	6, 8, 10a, 11	4.37, <i>d</i> (4.7)	87.1	6	6, 8, 8a, 10a, 11, 12	4.33, <i>d</i> (4.7)	86.7	6	6, 8, 10a, 11
6	2.72, <i>m</i>	28.7	5, 7, 11		2.86, <i>m</i>	28.7	5, 7, 11	8, 11	2.82, <i>m</i>	27	5, 7, 11	
7	2.25, <i>dd</i> (9.2, 17.9)	35.4	6, 7	5, 6, 8, 11	2.77, <i>dd</i> (9.4, 17.8)	35.9	6, 7	5, 6, 8, 11	2.74, <i>dd</i> (9.3, 17.7)	34.8	6, 7	5, 6, 8, 11
	1.93, <i>dd</i> (4.3, 17.9)				2.23, <i>dd</i> (5.5, 17.8)				2.19, <i>dd</i> (5.5, 17.7)			
8		175.9				175.7				175.6		
8a	3.18, <i>d</i> (17.2)	37.1	8a	5, 9, 9a, 10a, 12	3.16, <i>d</i> (17.5)	38.6	8a	5, 9, 9a, 10a, 12	3.15, <i>d</i> (17.4)	37.6	8a	5, 9, 10a, 12
	2.83, <i>d</i> (17.2)				3.05, <i>d</i> (17.3)				2.93, <i>d</i> (17.4)			
9		197.5				197.6				196.6		
9a		106.6				106.6				105.7		
10a		83.8				83.8				82.8		
11	1.02, <i>d</i> (7.0)	20.4	6	5, 6, 7	1.16, <i>d</i> (6.8)	20	6	5, 6, 7	1.12, <i>d</i> (6.8)	19.4	6	5, 6, 7
12	3.66, <i>d</i> (4.7)	61.3	12-OH	5, 8a, 10a	3.71, <i>dd</i> (5.1, 11.6)	62.5	12, 12-OH	5, 8a, 10a	3.65, <i>dd</i> (4.9, 11.7)	62.2	12, 12-OH	5, 8a, 10a
					3.65, <i>dd</i> (5.2, 11.8)				3.63, <i>dd</i> (4.9, 11.7)			
1-OH	12.01, <i>s</i>		12	1, 2, 9a	11.97, <i>s</i>		12	1, 2, 9a	11.95, <i>s</i>		12	1, 2, 9a
12-OH	5.35, <i>t</i> (5.0)		10a	10a	5.49, <i>t</i> (5.2)		10a, 12	10a, 12	5.47, <i>t</i> (5.0)		10a	10a
1'		160				158.8				159.2		
2'	6.50, <i>d</i> (8.5)	107.9	3'	1', 4', 9a'	6.50, <i>d</i> (8.8)	108.1	3'	1', 4', 9a'	7.33, <i>d</i> (8.5)	115.6	4'	1', 2, 4a'
3'	7.37, <i>d</i> (8.5)	139.8	2'	1', 2, 4a'	7.33, <i>d</i> (8.5)	139.8	2'	1', 2, 4a'	6.47, <i>d</i> (8.5)	136.2	3'	2', 4a', 9a'
4'		115.1				115.3				105.6		
4a'		156.1				156.1				157.2		
5'	4.39, <i>d</i> (4.7)	87.4	6'	6', 8', 10a', 11'	4.22, <i>d</i> (3.9)	86.3	6'	6', 8', 10a', 11'	4.33, <i>d</i> (4.7)	86.7	6'	6', 8', 10a', 11'
6'	2.87, <i>m</i>	28.6	5', 7', 11'		2.51, <i>m</i>	28.2	5', 7', 11'		2.82, <i>m</i>	27	5', 7', 11'	
7'	2.78, <i>dd</i> (9.4, 17.8)	35.9	6', 7'	5', 6', 8', 11'	2.13, <i>dd</i> (9.4, 17.9)	35.4	6', 7'	5', 6', 8', 11'	2.74, <i>dd</i> (9.3, 17.7)	34.8	6', 7'	5', 6', 8', 11'
	2.20, <i>dd</i> (5.4, 17.8)				1.96, <i>dd</i> (4.7, 17.9)				2.19, <i>dd</i> (5.5, 17.7)			
8'		175.7				175.9			–	175.6		
8a'	3.10, <i>d</i> (17.3)	38.8	8a'	5', 9', 10a', 12'	3.21, <i>d</i> (17.3)	38.3	8a'	5', 9', 9a', 10a', 12'	3.15, <i>d</i> (17.4)	37.6	8a'	5', 9', 10a', 12'
	3.06, <i>d</i> (17.3)				2.86, <i>d</i> (17.1)				2.93, <i>d</i> (17.4)			
9'		197.7				197.7				196.6		
9a'		107.1				106.9				105.7		
10a'		83.6				83.7				82.8		
11'	1.15, <i>d</i> (6.8)	20	6'	5', 6', 7'	1.01, <i>d</i> (7.0)	20.2	6'	5', 6', 7'	1.12, <i>d</i> (6.8)	19.4	6'	5', 6', 7'
12'	3.75, <i>dd</i> (5.0, 11.7)	62.1	12', 12'-OH	5', 8a', 10a'	3.66, <i>dd</i> (5.0, 11.6)	61.6	12', 12'-OH	5, 8a', 10a'	3.65, <i>dd</i> (4.9, 11.7)	62.2	12', 12'-OH	5', 8a', 10a'
	3.66, <i>dd</i> (5.0, 11.7)				3.58, <i>dd</i> (5.3, 11.6)				3.63, <i>dd</i> (4.9, 11.7)			
1'-OH	11.74, <i>s</i>		12'	1', 2', 9a'	11.72, <i>s</i>		12'	1', 2', 9a'	11.95, <i>s</i>		12'	1', 2', 9a'
12'-OH	5.45, <i>t</i> (5.3)		10a'	10a'	5.43, <i>t</i> (5.2)		10a', 12'	10a', 12'	5.47, <i>t</i> (5.0)		12'	10a'

^aChemical shifts deduced from HMBC correlations.

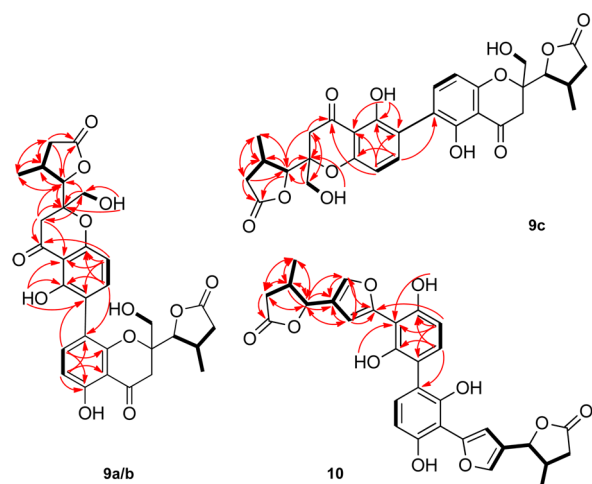


Figure 7. Key COSY (bold black bonds) and HMBC (red arrows) correlations in **9a–c** and **10**.

were coupled to the corresponding tertiary methine protons (H6/H6') with coupling constants of $J_{5,6} = 3.6$ Hz and $J_{5',6'} = 4.7$ Hz, characteristic of *trans*-oriented protons in these ring systems.⁶⁴ This finding was supported by detailed analysis of the ROESY spectrum, which showed strong correlations between H5/H5' and the methyl protons (11-CH₃/11'-CH₃), thus unambiguously confirming their *cis* orientation. In addition, the ROESY correlations between the methylene groups 12-CH₂/12'-CH₂ and H8a β /H8a' β , H5/H5', H6/H6' and 11-CH₃/11'-CH₃ as well as the absence of strong correlations to 7-CH₂/7'-CH₂ indicated an α orientation of the 3-methyl- γ -butyrolactone rings, as reported for the structurally related compound blennolide E.⁶⁵

Compound **9b** showed UV, HR-ESI-MS, and 1D and 2D NMR spectra (Figure 7) that were almost identical to those of **9a**. The presence of the same sets of signals in the ¹H and ¹³C NMR spectra indicated the same dimeric structural scaffold. Furthermore, ROESY spectra of **9b** revealed the same relative stereochemistry as in **9a**. However, the distinct difference in the

measured $[\alpha]_D$ values (+6° for **9a** and -28° for **9b**) indicated stereochemical differences between the two molecules. Their solution ECD spectra had opposite CEs below 330 nm and positive CEs at about 350 nm, which suggested that they are atropodiastereomers with the same absolute configuration in the chromanone ring. In contrast to **9a** and **9b**, compound **9c** showed only one set of ¹H and ¹³C NMR signals (Table 4), indicating a symmetrical dimer. Analysis of the 2D NMR spectra (Figure 7) revealed the same monomeric building units as in **9a** and **9b**. However, a 2,2'-linkage within the biaryl system was established by the HMBC correlations observed from H4/H4' to C2/C2', C4a/C4a', and C9a/C9a'; from H3/H3' to C1/C1', C2'/C2, and C4a/C4a'; and from 1/1'-OH to C1/C1', C2/C2', and C9a/C9a'. On the basis of the $[\alpha]_D$ value ($[\alpha]_D^{20} = -68^\circ$) and the ROESY spectrum, which showed the same correlations as observed for **9a** and **9b**, the relative configuration of **9c** was established as depicted in Figure 1.

The molecular formula of **10** was determined from HR-ESI-MS data as C₃₀H₂₆O₁₀ (m/z 547.1603 [M + H]⁺), implying 18 degrees of unsaturation as well as molecular weight decreases of 204 and 36 amu relative to **1** and **9a–c**, respectively. Detailed analysis of the NMR spectra of **10** revealed that the compound is a symmetrical dimer (Table 5 and Figure 7). Furthermore, comparison of the 1D and 2D NMR spectral data of **10** to those of **9c** illustrated similar structural features of the two compounds. The symmetrical biaryl system, including four *ortho*-coupled protons at δ_H 6.94 (H3/H3') and 6.51 (H2/H2'), as well as the 3-methyl- γ -butyrolactone moieties were retained in **10**. The corresponding signals of the tertiary methine, methylene, and oxymethine protons of the lactone moieties appeared at δ_H 2.65 (H6/H6'), 2.76/2.43 [(H7)₂/(H7')₂], and 5.05 (H5/H5'), respectively. A significant difference in the ¹H NMR spectrum of **10** compared with that of **9c** was the disappearance of the methylene groups 8a-CH₂/8a'-CH₂ and 12-CH₂/12'-CH₂ and the presence of two additional signals at δ_H 6.66 (H8a/H8a') and 7.82 (H12/H12') that were assigned to the olefinic protons. The ¹³C NMR spectrum of **10** showed 15 signals, corresponding to two carbonyl carbons at δ_C 176.0 (C8/C8'); 20 olefinic carbons at

Table 5. ¹H and ¹³C NMR, COSY, and HMBC Data for **10** at 600 (¹H) or 100 (¹³C) MHz (DMSO-*d*₆, δ in ppm, *J* in Hz)

atom	δ_H	δ_C	COSY ^a	HMBC ^a
1/1'		155.4		
2/2'	6.51, <i>d</i> (8.3)	107.4	3	1, 4, 9, 9a
3/3'	6.94, <i>d</i> (8.4)	131.8	2	1, 4', 4a
4/4'		118.5		
4a/4a'		152.1		
5/5'	5.05, <i>d</i> (8.7)	80.3	6, 12	6, 7, 8a, 10a, 11, 12
6/6'	2.65, <i>m</i>	36.9	5, 7, 11	5, 7, 10a, 11
7/7'	2.76, <i>dd</i> (7.9, 17.0) 2.43, <i>dd</i> (10.3, 17.0)	36.6	6, 7	5, 6, 8, 11
8/8'		176.0		
8a/8a'	6.66, <i>s</i>	109.3	12	5, 9, 10a, 12
9/9'		149.3		
9a/9a'		106.8		
10a/10a'		123.5		
11/11'	1.10, <i>d</i> (6.5)	15.9	6	5, 6, 7
12/12'	7.82, <i>s</i>	139.7	5, 8a	8a, 10a, 9
1/1'-OH	9.6, <i>s</i>			9a
4a/4a'-OH	9.48, <i>s</i>			9a

^aCorrelations are listed for only one monomeric building unit.

δ_C 155.4 (C1/C1'), 152.1 (C4a/C4a'), 149.3 (C9/C9'), 139.7 (C12/C12'), 131.8 (C3/C3'), 123.5 (C10a/C10a'), 118.5 (C4/C4'), 109.3 (C8a/C8a'), 107.4 (C2/C2'), and 106.8 ppm (C9a/9a'); two oximethines at δ_C 80.3 (C5/C5'); and six aliphatic carbons at δ_C 36.9 (C6/C6'), 36.6 (C7/C7'), and 15.9 (C11/C11'). The HMBC spectrum (Figure 7) disclosed correlations of H8a/H8a' and H12/H12' to C12/C12' and C8a/C8a', respectively, and to both C9/C9' and C10a/C10a'. These data allowed the construction of two furan rings located between the already identified structural elements, as evidenced by 3J correlations from H8a/H8a' to C5/C5' and H6/H6' to C10a/C10a' and by 4J correlations from the aromatic protons H2/H2' to C9/C9'. Furthermore, the 4,4'-linkage of the aromatic rings in **10** was deduced from the strong 3J correlations of H3 and H3' to C4' and C4, respectively. In analogy to **9a–c**, strong ROESY correlations between the oxymethine protons (H5/H5') and the methyl groups (11-CH₃/11'-CH₃) confirmed the *trans* orientation of H5/H5' and H6/H6' in the terminal lactone rings.

Initial experiments employing a crude EtOAc extract of *P. longicolla* following cultivation on rice resulted in complete inhibition of the growth of the murine lymphoma cell line L5178Y (at a dose of 10 $\mu\text{g/mL}$), as indicated by an MTT assay (data not shown). When compounds **1–11** were assayed for their activity in the same cell line (Table 6), the dimeric

Table 6. Cytotoxic Activities of the Isolated Compounds

compound	L5178Y growth (%) (conc = 10 $\mu\text{g/mL}$)	IC ₅₀ (μM) ^a
1	1.2	0.3
2	6.6	10
3	0.5	1.1
4	0.5	2.8
5	85.6	
6	92.6	
7	100	
8	100	
9a	90.7	
9b	97.4	
9c	89.2	
10	100	
11	100	

compound	IC ₅₀ (μM) in Various Cell Lines ^{a,b}					
	Cal27		Kyse510		A2780	
	sens	CisR	sens	CisR	sens	CisR
1	5.2	5.6	0.8	0.8	0.7	0.9
Cisplatin	7.8	41.4	2.5	8.4	1.2	10.2

Selectivity of 1			
cell line	DG75	Jurkat	PBMC
IC ₅₀ (μM) ^c	0.1	0.5	61.2

^aIncubation for 72 h. ^bAbbreviations: sens, sensitive to cisplatin; CisR, cisplatin-resistant. ^cIncubation for 48 h.

tetrahydroxanthone derivatives (**1–4**) were found to be active, with IC₅₀ values in the range 0.3–10 μM (Table 6). These results were in accordance with the published cytotoxic activity of **1** toward mouth epidermal carcinoma (KB) and lymphoma (BC1) cells and of **2** and **3** against lung (A549) and colon (HCT116) carcinoma cells.^{44,45} The remaining compounds showed no activity. The 4,4'-linked substances phomoxanthone A (**1**) and 12-deacetylphomoxanthone A (**4**) featured IC₅₀

values of 0.3 and 2.8 μM , respectively, whereas values of 1.1 and 10.0 μM were detected for the corresponding 2,2'-linked derivatives dicerandrol C (**3**) and dicerandrol B (**2**), respectively. These results indicated that the cytotoxic potential of this class of compounds is enhanced by a 4,4'-linkage of the tetrahydroxanthone monomers (**1** vs **3**) and decreased upon loss of acetyl groups (**1** vs **4** and **11**; **2** vs **3**). Deacetylphomoxanthone A (**11**) showed no activity against L5178Y mouse lymphoma cells, which may at least partly be due to the lower lipophilicity and hence hindered transmembrane diffusion of the deacetylated compound compared with the acetylated phomoxanthone A (logP = 2.230 for **1** vs logP = 0.125 for **11**). Alternatively, phomoxanthone A (**1**) may have a favored pharmacophore, whereas the deacetylated congener **11** may have no or less affinity to the respective target. The structural modifications of phomoxanthone A (**1**) caused by alkaline hydrolysis to afford compounds **9a–c** and **10** resulted in complete loss of activity (Table 6), implying that the dimeric tetrahydroxanthone core structure is mandatory for cytotoxic activity. Phomoxanthone A (**1**), which proved to be the most active compound isolated in this study, was subjected to further in vitro assays using different human cancer cell lines, including both cisplatin-sensitive and -resistant cells (Table 6). The chosen cell lines included the human ovarian carcinoma A2780, human tongue Cal27, and human esophagus Kyse510 cell lines. Remarkably, **1** showed almost the same potency against both anticancer-drug-sensitive and -resistant cell lines (Table 6). In order to probe the selectivity of **1** against cancer cells versus normal cells, we tested its effect on the human Burkitt's lymphoma cell line DG75 and the human T cell lymphoma cell line Jurkat versus healthy human peripheral blood mononuclear cells (PBMCs). The results showed that **1** is highly selective against cancer cells, as it is over 100-fold less toxic to PBMCs (IC₅₀ = 61.2 μM) compared with DG75 (IC₅₀ = 0.1 μM) and Jurkat (IC₅₀ = 0.5 μM) (Table 6).

In order to characterize the cytotoxic effect of the dimeric tetrahydroxanthone derivatives in more detail with regard to their mode of action, we analyzed the apoptosis-inducing potential of the lead compound phomoxanthone A (**1**) for the first time. Apoptosis is the programmed form of cell death, and it is central to many developmental and immunological processes. It is accompanied by specific molecular events, including the activation of aspartate-directed cysteine proteases (caspases) or fragmentation of chromosomal DNA. First we assessed the amount of apoptotic hypodiploid nuclei upon phomoxanthone A treatment of human DG75 B lymphocytes or Jurkat T lymphocytes. Hypodiploid nuclei are indicative of DNA fragmentation caused by the activation of caspases. Phomoxanthone A (**1**) significantly increased the amount of hypodiploid nuclei in both cell lines at a concentration of 1 μM (Figure 8A). This effect could be entirely blocked by the addition of the caspase inhibitor *N*-(2-quinolyl)valyl-aspartyl-(2,6-difluorophenoxy)methyl ketone (Q-VD-OPh) (Figure 8A). Next, we analyzed the activation of caspases by detection of the proteolytic processing of the caspase substrate poly(ADP-ribose) polymerase (PARP) by immunoblotting. Cleavage of PARP could be detected in both DG75 B cells and Jurkat T cells upon phomoxanthone A treatment, and again this effect could be entirely blocked by the addition of Q-VD-OPh (Figure 8B). Finally, we assessed the apoptosis-inducing capacities of compounds **1–11** by flow cytometric analyses of hypodiploid nuclei in Jurkat T cells. The dimeric tetrahydroxanthone derivatives were the most potent substances, thus

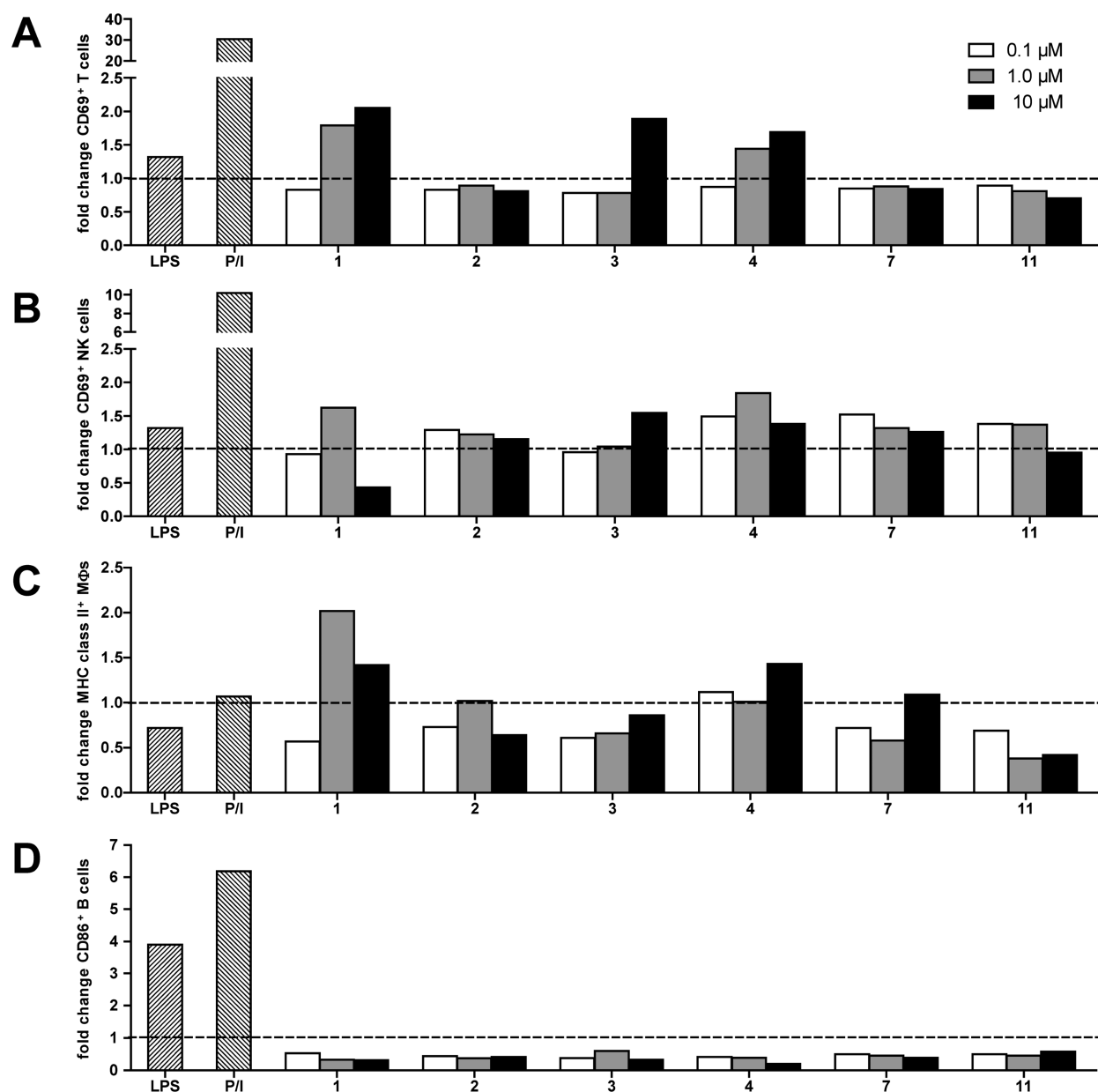


Figure 9. Immunostimulatory capacities of selected tetrahydroxanthone derivatives. Single cell suspensions from whole spleens of C57BL/6 mice were incubated for 12 h with the indicated concentration of 1–4, 7, or 11, 0.1% DMSO (negative control), LPS (positive control), or PMA and ionomycin (P/I; positive control). Cell activation was measured by flow cytometry as the expression of the surface markers CD69 on T cells (A) and NK cells (B), MHC class II on MΦs (C), and CD86 on B cells (D), and the results are given as fold increase relative to the DMSO negative control. Shown are one representative of two independent experiments for 2–4, 7, and 11 and of three independent experiments for 1.

acetyl groups (11) blunted the activation ability of the 4,4'-linked dimers. The positive correlation of lipophilicity with the T cell activation capacity of the substances (1 vs 11) indicates the necessity of passing cellular membrane compartments rather than an interaction with cell-surface molecules as the underlying mechanism of activation. Similar relative activation potentials for the studied substances could be found for primary murine NK cells and macrophages (MΦ), as measured by upregulation of CD69 and MHC class II, respectively, while none of the compounds tested were able to induce upregulation of the costimulatory molecule CD86 on primary murine B lymphocytes (Figure 9B–D). Accordingly, in addition to their direct cytotoxic and pro-apoptotic activities on tumor cells, as shown above, the 4,4'-linked dimeric tetrahydroxanthones 1 and 4 exhibit an intrinsic immunostimulatory capacity on

primary nontransformed T cells, NK cells, and MΦ by yet unknown signal transduction pathways. This dual activity offers interesting synergistic mechanisms to increase the efficiency of cancer treatment and to counteract the establishment of resistance pathways in cancer cells, making phomoxanthone A (1) an interesting candidate for further studies.

CONCLUSION

This study has revised the structure of the previously reported compound phomoxanthone A (1) as being (aR,5S,6-S,10aS,5'S,6'S,10a'S). In addition, the absolute configurations of dicerandrol B (2), dicerandrol C (3), and 12-deacetylphomoxanthone (4) were established for the first time. The marked cytotoxicity of 1 against a set of cancer cell lines, including

some cisplatin-resistant ones, was shown to be due to induction of apoptosis. The significant difference of activity of **1** against cancer cells versus healthy blood cells makes this compound an interesting candidate for further studies. Furthermore, **1** was shown to be a potent activator of murine T cells, NK cells, and macrophages, suggesting activation of the immune system, which would help to eradicate any tumor cells surviving chemotherapeutic treatment. The location of the biaryl axis in the investigated tetrahydroxanthone dimers (**1–4**) and the presence of acetyl groups were identified as being important structural elements that influence the biological activities of the studied compounds.

EXPERIMENTAL SECTION

General Experimental Procedures. Fractions and pure compounds were analyzed on an HPLC system coupled to a photodiode array detector, and routine detection was performed at 235, 254, 280, and 340 nm. Separation was carried out over a C18 reversed-phase column (5 μm ; 125 mm \times 4 mm length \times i.d.), and the following linear gradient was used: 0.02% H_3PO_4 in H_2O and MeOH; flow rate 1.0 mL/min. Final purification was performed on a semipreparative HPLC system with a C18 reversed-phase column (5 μm ; 300 mm \times 8 mm, length \times i.d.), flow rate 5.0 mL/min. 1D and 2D NMR spectra were recorded on 600 or 500 MHz NMR spectrometers. HRMS analysis was recorded on a Q-TOF mass spectrometer in ESI mode. Solvents were distilled prior to use, and spectral-grade solvents were used for spectroscopic measurements.

Fungal Material and Cultivation. The fungal strain *P. longicolla* was isolated from fresh healthy leaves of the mangrove tree *S. caseolaris* that were collected in October 2005 in Dong Zhai Gang-Mangrove Garden on Hainan Island, P. R. China, using a protocol previously described.⁶⁶ *P. longicolla* was taxonomically identified according to a previously described method.^{67,68} The sequence data has been submitted to GenBank with accession number AY857868.1. The fungus was cultivated on solid rice medium (to 100 g of commercially available rice was added 100 mL of distilled water and kept overnight prior to autoclaving) at room temperature under static conditions.^{67,68}

Extraction and Isolation. The solid rice culture of *P. longicolla* was overlaid and extracted with EtOAc, and then the solvent was removed under reduced pressure. The crude extract (24.9 g) was washed with distilled water and then fractionated between MeOH 90% and *n*-hexane. The MeOH fraction (16.4 g) was then subjected to Diaion HP-20 and eluted using a stepwise gradient system from 100% H_2O to 100% MeOH and from 1:1 MeOH/acetone to 100% acetone. Promising fractions were subjected to further chromatographic separation using Diaion HP-20 with H_2O , MeOH, and acetone as eluting solvents; silica (VLC) with a stepwise gradient system from 100% *n*-hexane to 100% EtOAc and from 100% DCM to 100% MeOH; or Sephadex LH-20 (100% MeOH or 1:1 DCM/MeOH). If necessary, final purification was performed by semipreparative HPLC to yield **1** (3.4 g), **2** (5.3 mg), **3** (3.2 mg), **4** (6.1 mg), **5** (3.9 mg), **6** (3.1 mg), **7** (2.1 mg), and **8** (5.4 mg).

Phomoxanthone A (1). Yellowish amorphous granules. $[\alpha]_{\text{D}}^{20} = +83$ (c 0.3, CHCl_3). UV λ_{max} (PDA): 218, 258, 333 nm. ECD (MeCN, $c = 1.10 \times 10^{-4}$) $\lambda_{\text{max}}/\text{nm}$ ($\Delta\epsilon$): 341 (−7.79) with a flat negative plateau up to 420 nm, 316 (17.65), 275 (−3.49), 257 (1.33), 228 (−46.79), 208 (−66.22), positive below 197 nm. ECD (86 μg of **1** in 250 mg of KCl) $\lambda_{\text{max}}/\text{nm}$ ($\Delta\epsilon$): 350 (19.16), 324 (32.71), 278 (−2.77), 258 (11.57), 227 (−87.44), 209 (−122.92), positive below 197 nm.

Dicerandrol B (2). Yellow amorphous powder. $[\alpha]_{\text{D}}^{20} = -25$ (c 0.4, CHCl_3). UV λ_{max} (PDA): 215, 258, 338 nm. ECD (MeCN, $c = 1.30 \times 10^{-4}$) $\lambda_{\text{max}}/\text{nm}$ ($\Delta\epsilon$): 373 br (6.08), 344 sh (2.09), 328 sh (2.11), 268 sh (−6.42), 233 (−13.74), 198 (−13.2).

Dicernadrol C (3). Yellow amorphous powder. $[\alpha]_{\text{D}}^{20} = -17$ (c 0.1, CHCl_3). UV λ_{max} (PDA): 212, 260, 340 nm. ECD (MeCN, $c = 0.99 \times 10^{-4}$) $\lambda_{\text{max}}/\text{nm}$ ($\Delta\epsilon$): 375 sh (−3.61), 365 (−3.70), 324 (9.01), 297 sh (2.55), 258 sh (−9.25), 233 (−16.57), 202 (−14.13).

12-Deacetylphomoxanthone (4). Yellow amorphous powder. $[\alpha]_{\text{D}}^{20} = +35$ (c 0.2, MeOH). UV λ_{max} (PDA): 221, 259, 337 nm. ECD (MeCN, $c = 1.26 \times 10^{-4}$) $\lambda_{\text{max}}/\text{nm}$ ($\Delta\epsilon$): 346 br (19.19), 300 (−0.71), 277 (−0.62), 252 (7.07), 226 sh (−56.48), 211 (−62.70). ^1H and ^{13}C NMR: Table 1. HR-ESI-MS: m/z 709.2127 $[\text{M} + \text{H}]^+$ (calcd for $\text{C}_{36}\text{H}_{37}\text{O}_{15}$, 709.2127).

Phomo-2,3-dihydrochromone (5). Brown amorphous mass. UV λ_{max} (PDA): 215, 250, 345 nm. ^1H and ^{13}C NMR: Table 2. HR-ESI-MS: m/z 289.0707 $[\text{M} + \text{H}]^+$ (calcd for $\text{C}_{15}\text{H}_{13}\text{O}_6$, 289.0707).

Isomonodictyphenone (6). Yellowish powder. UV λ_{max} (PDA): 209, 286 nm. ^1H and ^{13}C NMR: Table 3. HR-ESI-MS: m/z 289.0703 $[\text{M} + \text{H}]^+$ (calcd for $\text{C}_{15}\text{H}_{13}\text{O}_6$, 289.0707).

Structural Derivatization of Phomoxanthone A. Alcoholic Alkaline Hydrolysis. A solution of phomoxanthone A (**1**) (30 mg) in ethanolic NaOH (5 mL, 0.5 N) was stirred for 4 h at 23 °C, followed by dropwise treatment with hydrochloric acid (37 wt %). When the pH reached 4, the solution was neutralized with sodium bicarbonate (q.s.). Water (100 mL) was added, and the aqueous dilution was extracted three times with EtOAc (30 mL). The combined solvent extracts were evaporated to dryness. The obtained mixture was purified by semipreparative HPLC to yield **9a** (5.6 mg), **9b** (4.0 mg), and **9c** (9.4 mg).

Hydrolysis Product I (9a). Brownish amorphous powder. $[\alpha]_{\text{D}}^{20} = +6$ (c 1.1, DMSO). UV λ_{max} (PDA): 251, 360 nm. ECD (MeCN, $c = 2.86 \times 10^{-4}$) $\lambda_{\text{max}}/\text{nm}$ ($\Delta\epsilon$): 357 sh (0.39), 306 sh (2.08), 285 (3.78), 258 (−0.15), 237 (3.57), 208 (−8.05). ^1H and ^{13}C NMR: Table 4. HR-ESI-MS: m/z 583.1810 $[\text{M} + \text{H}]^+$ (calcd for $\text{C}_{30}\text{H}_{31}\text{O}_{12}$, 583.1810).

Hydrolysis Product II (9b). Brownish amorphous powder. $[\alpha]_{\text{D}}^{20} = -28$ (c 0.8, DMSO). UV λ_{max} (PDA): 250, 359 nm. ECD (MeCN, $c = 2.86 \times 10^{-4}$) $\lambda_{\text{max}}/\text{nm}$ ($\Delta\epsilon$): 351 (1.23), 306 sh (−1.76), 283 (−2.77), 237 (−3.06), 206 (4.01). ^1H and ^{13}C NMR: Table 4. HR-ESI-MS: m/z 583.1810 $[\text{M} + \text{H}]^+$ (calcd for $\text{C}_{30}\text{H}_{31}\text{O}_{12}$, 583.1810).

Hydrolysis Product III (9c). Brownish amorphous powder. $[\alpha]_{\text{D}}^{20} = -68$ (c 0.9, DMSO). UV λ_{max} (PDA): 252, 363 nm. ECD (MeCN, $c = 2.86 \times 10^{-4}$) $\lambda_{\text{max}}/\text{nm}$ ($\Delta\epsilon$): 356 (1.01), 285 (0.34), 266 (−0.37), 236 (2.43), 208 (−5.67). ^1H and ^{13}C NMR: Table 4. HR-ESI-MS: m/z 583.1810 $[\text{M} + \text{H}]^+$ (calcd for $\text{C}_{30}\text{H}_{31}\text{O}_{12}$, 583.1810).

Aqueous Alkaline Hydrolysis. A solution of phomoxanthone A (**1**) (50 mg) in aqueous NaOH solution (100 mL, 0.5 N) was heated under reflux for 1 h. After the mixture was cooled, the pH was adjusted to 5 with hydrochloric acid (37 wt %), and the mixture was extracted three times by shaking with 30 mL of EtOAc. The combined solvent extracts were evaporated to dryness. The obtained mixture was purified by semipreparative HPLC to yield **10** (4.8 mg).

Hydrolysis Product IV (10). Brownish amorphous powder. $[\alpha]_{\text{D}}^{20} = -127$ (c 0.5, DMSO). UV λ_{max} (PDA): 215, 260 nm. ^1H and ^{13}C NMR: Table 5. HR-ESI-MS: m/z 547.1603 $[\text{M} + \text{H}]^+$ (calcd for $\text{C}_{30}\text{H}_{27}\text{O}_{10}$, 547.1599).

Cell Proliferation Assay. Cytotoxicity was tested against the L5178Y mouse lymphoma cell line using the MTT assay [MTT = 3-(4,5-dimethylthiazol-2-yl)-2,5-diphenyl-2H-tetrazolium bromide].^{69,70} Furthermore, the cytotoxicity was evaluated against the human ovarian carcinoma cell line A2780, the human tongue cell line Cal27, the human esophagus cell line Kyse510, the human T cell lymphoma cell line Jurkat, and the human Burkitt's lymphoma cell line DG75 by an MTT assay as previously described, except that for Jurkat and DG75, incubation with DMSO at RT for 20 min was used to extract the formazan product from the cells.⁷¹ The A2780 cell line was obtained from the European Collection of Cell Cultures (ECACC, Salisbury, UK). The Cal27 and Kyse510 cell lines as well as Jurkat (no. ACC-282) and DG75 (no. ACC-83) were obtained from the German Collection of Microorganisms and Cell Cultures (DSMZ, Germany). The cisplatin-resistant (CisR) cell lines were generated by exposing the parental cell lines to weekly cycles of cisplatin in an IC_{50} concentration over a period of 24–30 weeks, as described by Gosepath et al.⁷² and Eckstein et al.⁷³ All of the cancer cell lines were grown at 37 °C under humidified air supplemented with 5% CO_2 in RPMI 1640 (A2780, Kyse510, Jurkat, DG75) or DMEM (Cal27) containing 10% fetal calf serum, 120 IU/mL penicillin, and 120 $\mu\text{g}/\text{mL}$ streptomycin. The medium for Jurkat and DG75 was additionally

supplemented with 1% HEPES. The cells were grown to 80% confluency before they were used for the cell proliferation assay.

The selectivity of phomoxanthone A (**1**) cytotoxicity was assessed on PBMCs by trypan blue exclusion assay. Different concentrations of **1** were used to treat cells while the negative control was treated with the same volume of DMSO. At each time course (24 and 48 h), 20 μL of the cell suspension was mixed with 20 μL of trypan blue, and 20 μL of this mixture was applied to a hemocytometer and observed by a binocular microscope. The unstained cells (viable) in the negative control and treated samples were counted, and the percentage of viability was calculated from three independent tests.

Apoptosis Assay. DG75 cells (Burkitt's lymphoma-derived human B cell line; DSMZ no. ACC-83) or Jurkat cells (leukemia-derived human T cell line; DSMZ no. ACC-282) were cultivated in medium containing the indicated concentrations of compounds for 24 h, and apoptosis was measured. Nuclei were prepared by lysing cells in hypotonic lysis buffer (1% sodium citrate, 0.1% Triton X-100, 50 $\mu\text{g}/\text{mL}$ propidium iodide) and subsequently analyzed by flow cytometry using FACSDiva software. Nuclei to the left of the 2 N peak were considered as apoptotic.

Cell Extracts and Immunoblotting. DG75 B cells or Jurkat T cells were treated with the different compounds at the indicated concentrations for the indicated times. Cells were lysed in lysis buffer [20 mM Tris-HCl, pH 7.5, 150 mM NaCl, 0.5 mM EDTA, 1% Triton X-100, 10 mM NaF, 2.5 mM NaPP₆, 10 μM Na₂MoO₄, 1 mM Na₃VO₄, protease inhibitors (P2714)], and the lysates were clarified by centrifugation at 16000g for 10 min. Equal total protein amounts, as determined by Bradford, were separated on 10% SDS-polyacrylamide gels and transferred to a PVDF membrane. Immunoblot analysis was performed using primary mouse antibodies to PARP (no. BML-SA250) or β -actin (no. A5316) and IRDye800- or IRDye680-conjugated secondary antibodies. Signals were detected with an infrared imaging system.

FACS Analysis of Immune Cell Activation Markers. Spleens of female C57BL/6 mice were digested with collagenase VIII and DNase I and homogenized using a cell strainer. Cell suspensions were incubated with the indicated compounds for 12 h in DMSO as 1:100 dilutions in medium at the indicated final concentrations. As positive controls, cells were stimulated for 12 h with 10 ng/mL PMA and 500 ng/mL ionomycin or 100 ng/mL LPS (*Salmonella Minnesota*, List Laboratories). For FACS analysis cells, were labeled with the following antibodies: CD11b (M1/70), B220 (Ra3-6B2), CD11c (HL3), CD3e (145-2C11), CD19 (1D3), CD86 (GL1), CD69 (H1.2F3), MHC class II (AF6-120.1), and CD49 (DX5). DAPI was added for dead cell discrimination. Samples were acquired on a flow cytometer and analyzed with FlowJo software. T lymphocytes were defined as CD3e⁺CD49⁻, B lymphocytes as B220⁺CD11c⁻, NK cells as CD49⁺CD3e⁻, and M Φ s as CD11b⁺CD11c⁻.

X-ray Crystallography. Single crystals of phomoxanthone A (**1**) suitable for X-ray diffraction were crystallized from EtOAc at room temperature. A single crystal was mounted on a loop under a polarizing microscope. Data for compound **1** were collected as follows: diffractometer (with microfocus tube), Cu K α radiation ($\lambda = 1.54178$ Å), 123 ± 2 K, multilayer mirror, ω and ϕ scan, data collection with Apex2,⁷⁴ cell refinement and data reduction with SAINT,⁷⁴ and experimental absorption correction with SADABS.⁷⁵

The structure of **1** was solved by direct methods using SHELXS-97; refinement was done by full-matrix least-squares on F^2 using the SHELXL-97 program suite.⁷⁶ All non-hydrogen positions were refined with anisotropic displacement parameters. Hydrogen atoms of two hydroxyl groups, aromatic CH groups, and aliphatic CH, CH₂, and CH₃ groups were positioned geometrically (O–H = 0.84 Å for OH; C–H = 0.95 Å for aromatic CH; C–H = 1.00 Å for aliphatic and olefinic CH; C–H = 0.99 Å for CH₂; C–H = 0.98 Å for CH₃) and refined using riding models with $U_{\text{iso}}(\text{H}) = 1.2U_{\text{eq}}(\text{C}, \text{CH}_2)$ and $U_{\text{iso}}(\text{H}) = 1.5U_{\text{eq}}(\text{O}, \text{CH}_3)$. Hydrogen atoms of the other two hydroxyl groups (C–OH) were found and refined with $U_{\text{iso}}(\text{H}) = 1.5U_{\text{eq}}(\text{O})$.

The absolute structure assignment was based on anomalous dispersion using the Flack parameter.^{48–51} Friedel opposites were not merged. The correct assignment in the absence of any heavy atoms

was checked by inverting the structure (MOVE 1 1 1 –1), which then led to a Flack parameter close to 1.

The crystal solvent molecules EtOAc and water in the channels of **1** were found to be highly disordered and could not be properly defined. Hence, the SQUEEZE option in PLATON for Windows^{77–80} was used to refine the framework structure without the disordered electron density in the voids. One EtOAc and one water molecule per unit cell were squeezed. With two phomoxanthone molecules in the unit cell, **1** should be named as phomoxanthone A hemi(ethyl acetate) hemihydrate. The SQUEEZE routine suggested a 277 Å³ (13.8%) cavity in the unit cell with a population of 87 electrons [roughly in agreement with 48 electrons for CH₃C(O)OC₂H₅ and 10 electrons for H₂O] for the solvated form. A PLATON^{77–80} void calculation for the solvent-free form with a probe radius of 1.2 Å gave a total potential solvent volume of 291 Å³ (14.5%).

The crystal structure is disordered at the O16 and C36 positions (the C=O moiety) as part of a torsional disorder of the acetyl group. The respective A atoms and B atoms were refined with about equal occupations, and A and B components were separated by a PART instruction. This torsional disorder is due to the presence of only very weak C–H \cdots O interactions in the packing diagram, allowing this moiety to assume two different orientations (Figure S7 in the Supporting Information). The displacement of the acetyl group does not affect and is independent of the absolute structure assignment.

Crystal data and details of the structure refinement are given in Table S1 in the Supporting Information. Graphics were drawn with DIAMOND,⁸¹ and analyses of the O–H \cdots O hydrogen bonds were performed with PLATON for Windows.^{77–80} The structural data have been deposited with the Cambridge Crystallographic Data Center (CCDC no. 937755).

■ COMPUTATIONAL SECTION

Mixed torsional/low-frequency mode conformational searches were carried out by means of the MacroModel 9.9.223 software using the Merck Molecular Force Field (MMFF) with an implicit solvent model for chloroform.⁸² Geometry reoptimizations were carried out at the B3LYP/6-31G(d) level in vacuo, the B3LYP/TZVP level with a PCM solvent model for acetonitrile, and the M06/TZVP level⁴⁷ with the PCM model for acetonitrile. TDDFT ECD calculations were run with various functionals (B3LYP, BHandHLYP, PBE0) and the TZVP basis set as implemented in the Gaussian 09 package.⁸³ Scans and TS calculations were carried out at the B3LYP/6-31G(d) level in vacuo. ECD spectra were generated as sums of Gaussians with 2400 and 3000 cm⁻¹ widths at half-height (corresponding to ca. 13 and 16 at 230 nm), using dipole-velocity-computed rotational strengths.⁸⁴ Boltzmann distributions were estimated from the ZPVE-corrected B3LYP/6-31G(d) energies in the gas phase calculations and from the B3LYP/TZVP and M06/TZVP energies in the solvated ones. For computation of the rotational barriers, the ZPVE-corrected B3LYP/6-31G(d) energies were applied. The MOLEKEL software package was used for visualization of the results.⁸⁵

■ ASSOCIATED CONTENT

● Supporting Information

Supplementary figures showing structures of the low- and high-energy transition states for the inversion of the C2–C2' bond of (5*R*,6*R*,10*aR*,5'*R*,6'*R*,10*a'**R*)-**2**, solution conformers and populations ($\geq 2\%$) of (5*R*,6*R*,10*aR*,5'*R*,6'*R*,10*a'**R*)-**2** and (5*R*,6*R*,10*aR*,5'*R*,6'*R*,10*a'**R*)-**3**, molecular structure of phomoxanthone A (**1**) with determined absolute configuration (different views), previous and redetermined absolute structures of phomoxanthone A (**1**), experimental and calculated ECD spectra of the nonoptimized “old” (a*S*,5*R*,6*R*,10*aR*,5'*R*,6'*R*,10*a'**R*) X-ray structures of **1** in vacuo, and section of the packing diagram of phomoxanthone A (**1**); supplementary tables showing crystal data and structure refinement for **1**, inter- and intramolecular interactions with lengths (Å) and angles

(deg) in **1**, and selected bond lengths (Å) and angles (deg) in **1**; references; description of the Flack parameter; thermal ellipsoid plots for **1**; ¹H and ¹³C NMR spectra of the new compounds (**4–6** and **9a–10**); and Cartesian coordinates of the low-energy reoptimized conformers of **2** and **3**, the low- and high-energy transition states for the inversion of the C2–C2' bond of **2**, and the optimized X-ray structures of **1**. This material is available free of charge via the Internet at <http://pubs.acs.org>.

AUTHOR INFORMATION

Corresponding Authors

*P.P.: Phone: 0049-211-8114163. Fax: 0049-211-8111923. E-mail: proksch@uni-duesseldorf.de.

*A.H.A.: Phone: 0049-211-8114173. E-mail: amal.hassan@uni-duesseldorf.de.

Notes

The authors declare no competing financial interest.

ACKNOWLEDGMENTS

Financial support by grants from BMBF to P.P. is gratefully acknowledged. T.K. and A.M. thank the Hungarian National Research Foundation (OTKA K105871) and the TÁMOP 4.2.4. A/2-11-1-2012-0001 National Excellence Program for financial support and the National Information Infrastructure Development Institute (NIIFI 10038) for CPU time. S.S. was supported by the Deutsche Forschungsgemeinschaft (SCHE692/3-1, SCHE692/4-1). R.S. was supported by an AFR Fellowship from the Fonds National de la Recherche in Luxembourg. Research at LBMCC was financially supported by the Fondation de Recherche Cancer et Sang, the Recherches Scientifiques Luxembourg Association, the Een Haerz fir kriebeskrank Kanner Association, the Action Lions Vaincre le Cancer Association, the European Union (ITN “RedCat” 215009, Interreg Iva Project “Corena”), and the Télévie Luxembourg. M.D. was supported by the National Research Foundation (NRF) of the MEST of Korea through a Tumor Microenvironment Global Core Research Center (GCRC) grant (2012-0001184), by a Seoul National University research grant, and by the Research Settlement Fund for New Faculty of SNU. We thank Prof. W. E. G. Müller (University of Mainz, Germany) for MTT analysis using the LS178Y cell line.

REFERENCES

- Halpin, H. A.; Morales-Suárez-Varela, M. M.; Martin-Moreno, J. M. *Public Health Rev.* **2010**, *32*, 120–154.
- Pritchard, J. R.; Lauffenburger, D. A.; Hemann, M. T. *Drug Resist. Updates* **2012**, *15*, 249–257.
- Loeb, K. R.; Loeb, L. A. *Carcinogenesis* **2000**, *21*, 379–385.
- Lippert, T. H.; Ruoff, H.-J.; Volm, M. *Arzneimittelforschung* **2008**, *58*, 261–264.
- Brichard, V. G.; Lejeune, D. *Expert Opin. Biol. Ther.* **2008**, *8*, 951–968.
- Mantovani, A.; Romero, P.; Palucka, A. K.; Marincola, F. M. *Lancet* **2008**, *371*, 771–783.
- Marincola, F. M.; Wang, E.; Herlyn, M.; Seliger, B.; Ferrone, S. *Trends Immunol.* **2003**, *24*, 334–341.
- Zitvogel, L.; Apetoh, L.; Ghiringhelli, F.; Andre, F.; Tesniere, A.; Kroemer, G. *J. Clin. Invest.* **2008**, *118*, 1991–2001.
- Kiladjian, J.-J.; Mesa, R. A.; Hoffman, R. *Blood* **2011**, *117*, 4706–4715.
- Newman, D. J.; Cragg, G. M. *J. Nat. Prod.* **2012**, *75*, 311–335.
- Bacon, C. W.; White, J. F. Coevolution of Fungal Endophytes with Grasses: The Significance of Secondary Metabolites. In *Microbial*

Endophytes; Bacon, C. W., White, J. F., Eds.; Marcel Dekker: New York, 2000; pp 341–388.

(12) Redman, R. S.; Sheehan, K. B.; Stout, R. G.; Rodriguez, R. J.; Henson, J. M. *Science* **2002**, *298*, 1581.

(13) Giordano, L.; Gonthier, P.; Varese, G. C.; Miserere, L.; Nicolotti, G. *Fungal Diversity* **2009**, *38*, 69–83.

(14) Bae, H.; Sicher, R. C.; Kim, M. S.; Kim, S.-H.; Strem, M. D.; Melnick, R. L.; Bailey, B. A. *J. Exp. Bot.* **2009**, *60*, 3279–3295.

(15) Singh, L. P.; Gill, S. S.; Tuteja, N. *Plant Signaling Behav.* **2011**, *6*, 175–191.

(16) Kharwar, R. N.; Mishra, A.; Gond, S. K.; Stierle, A.; Stierle, D. *Nat. Prod. Rep.* **2011**, *28*, 1208–1228.

(17) Lingham, R. B.; Silverman, K. C.; Bills, G. F.; Cascales, C.; Sanchez, M.; Jenkins, R. G.; Gartner, S. E.; Martin, I.; Diez, M. T.; Peláez, F.; Mochales, S.; Kong, Y.-L.; Burg, R. W.; Meinz, M. S.; Huang, L.; Nallin-Omstead, M.; Mosser, S. D.; Schaber, M. D.; Omer, C. A.; Pompliano, D. L.; Gibbs, J. B.; Singh, S. B. *Appl. Microbiol. Biotechnol.* **1993**, *40*, 370–374.

(18) Zhang, J.-Y.; Tao, L.-Y.; Liang, Y.-J.; Yan, Y.-Y.; Dai, C.-L.; Xia, X.-K.; She, Z.-G.; Lin, Y.-C.; Fu, L.-W. *Cell Cycle* **2009**, *8*, 2444–2450.

(19) Turbyville, T. J.; Wijeratne, E. M. K.; Liu, M. X.; Burns, A. M.; Seliga, C. J.; Luevano, L. A.; David, C. L.; Faeth, S. H.; Whitesell, L.; Gunatilaka, A. A. L. *J. Nat. Prod.* **2006**, *69*, 178–184.

(20) Kimura, T.; Nishida, M.; Kuramochi, K.; Sugawara, F.; Yoshida, H.; Mizushima, Y. *Bioorg. Med. Chem.* **2008**, *16*, 4594–4599.

(21) Kusari, S.; Hertweck, C.; Spiteller, M. *Chem. Biol.* **2012**, *19*, 792–798.

(22) Strobel, G.; Daisy, B. *Microbiol. Mol. Biol. Rev.* **2003**, *67*, 491–502.

(23) Klaiday, S.; Rukachaisirikul, V.; Tadpetch, K.; Sukpondma, Y.; Phongpaichit, S.; Buatong, J.; Sakayaroj, J. *Tetrahedron* **2012**, *68*, 2299–2305.

(24) Liu, D.; Li, X.-M.; Meng, L.; Li, C.-S.; Gao, S.-S.; Shang, Z.; Proksch, P.; Huang, C.-G.; Wang, B.-G. *J. Nat. Prod.* **2011**, *74*, 1787–1791.

(25) Xu, J.; Aly, A. H.; Wray, V.; Proksch, P. *Tetrahedron Lett.* **2011**, *52*, 21–25.

(26) Li, H.; Huang, H.; Shao, C.; Huang, H.; Jiang, J.; Zhu, X.; Liu, Y.; Liu, L.; Lu, Y.; Li, M.; Lin, Y.; She, Z. *J. Nat. Prod.* **2011**, *74*, 1230–1235.

(27) Debbab, A.; Aly, A. H.; Proksch, P. *Fungal Diversity* **2013**, *61*, 1–27.

(28) Udayanga, D.; Liu, X.; McKenzie, E. C.; Chukeatirote, E.; Bahkali, A. A.; Hyde, K. *Fungal Diversity* **2011**, *50*, 189–225.

(29) Dai, J.; Krohn, K.; Gehle, D.; Kock, I.; Flörke, U.; Aust, H.-J.; Draeger, S.; Schulz, B.; Rheinheimer, J. *Eur. J. Org. Chem.* **2005**, 4009–4016.

(30) Hussain, H.; Akhtar, N.; Draeger, S.; Schulz, B.; Pescitelli, G.; Salvadori, P.; Antus, S.; Kurtán, T.; Krohn, K. *Eur. J. Org. Chem.* **2009**, 749–756.

(31) Claydon, N.; Grove, J. F.; Pople, M. *Phytochemistry* **1985**, *24*, 937–943.

(32) Hussain, H.; Ahmed, I.; Schulz, B.; Draeger, S.; Krohn, K. *Fitoterapia* **2012**, *83*, 523–526.

(33) Krohn, K.; Hussain, H.; Egold, H.; Schulz, B.; Green, I. *ARKIVOC* **2012**, *2012* (vi), 71–89.

(34) Krohn, K.; Michel, A.; Römer, E.; Flörke, U.; Aust, H.-J.; Draeger, S.; Schulz, B.; Wray, V. *Nat. Prod. Lett.* **1995**, *6*, 309–314.

(35) Li, Y.-Y.; Wang, M.-Z.; Huang, Y.-J.; Shen, Y.-M. *Mycology* **2010**, *1*, 254–261.

(36) Lim, C.; Kim, J.; Choi, J. N.; Ponnusamy, K.; Jeon, Y.; Kim, S. U.; Kim, J. G.; Lee, C. *J. Microbiol. Biotechnol.* **2010**, *20*, 494–500.

(37) Lin, T.; Lin, X.; Lu, C.; Hu, Z.; Huang, W.; Huang, Y.; Shen, Y. *Eur. J. Org. Chem.* **2009**, 2975–2982.

(38) Nithya, K.; Muthumary, J. *Recent Res. Sci. Technol.* **2010**, *2*, 99–103.

(39) Rukachaisirikul, V.; Sommart, U.; Phongpaichit, S.; Sakayaroj, J.; Kirtikara, K. *Phytochemistry* **2008**, *69*, 783–787.

- (40) Talontsi, F. M.; Islam, M. T.; Facey, P.; Douanla-Meli, C.; von Tiedemann, A.; Laatsch, H. *Phytochem. Lett.* **2012**, *5*, 657–664.
- (41) Toyomasu, T.; Kaneko, A.; Tokiwano, T.; Kanno, Y.; Kanno, Y.; Niida, R.; Miura, S.; Nishioka, T.; Ikeda, C.; Mitsushashi, W.; Dairi, T.; Kawano, T.; Oikawa, H.; Kato, N.; Sassa, T. *J. Org. Chem.* **2009**, *74*, 1541–1548.
- (42) Izawa, Y.; Hirose, T.; Shimizu, T.; Koyama, K.; Natori, S. *Tetrahedron* **1989**, *45*, 2323–2335.
- (43) Elsässer, B.; Krohn, K.; Flörke, U.; Root, N.; Aust, H.-J.; Draeger, S.; Schulz, B.; Antus, S.; Kurtán, T. *Eur. J. Org. Chem.* **2005**, 4563–4570.
- (44) Isaka, M.; Jaturapat, A.; Rukseree, K.; Danwisetkanjana, K.; Tanticharoen, M.; Thebtaranonth, Y. *J. Nat. Prod.* **2001**, *64*, 1015–1018.
- (45) Wagenaar, M. M.; Clardy, J. *J. Nat. Prod.* **2001**, *64*, 1006–1009.
- (46) Andersen, R.; Buechi, G.; Kobbe, B.; Demain, A. L. *J. Org. Chem.* **1977**, *42*, 352–353.
- (47) Zhao, Y.; Truhlar, D. *Theor. Chem. Acc.* **2008**, *120*, 215–241.
- (48) Flack, H. *Acta Crystallogr., Sect. A* **1983**, *39*, 876–881.
- (49) Flack, H. D.; Bernardinelli, G. *Acta Crystallogr., Sect. A* **1999**, *55*, 908–915.
- (50) Flack, H. D.; Bernardinelli, G. *Chirality* **2008**, *20*, 681–690.
- (51) Flack, H. D.; Sadki, M.; Thompson, A. L.; Watkin, D. J. *Acta Crystallogr., Sect. A* **2011**, *67*, 21–34.
- (52) Krick, A.; Kehraus, S.; Gerhauser, C.; Klimo, K.; Nieger, M.; Maier, A.; Fiebig, H. H.; Atodiresi, I.; Raabe, G.; Fleischhauer, J.; König, G. M. *J. Nat. Prod.* **2007**, *70*, 353–360.
- (53) Asahina, Y.; Fujikawa, F. *Ber. Dtsch. Chem. Ges.* **1935**, *68*, 1558–1565.
- (54) Waser, M.; Lackner, B.; Zuschrader, J.; Müller, N.; Falk, H. *Tetrahedron Lett.* **2005**, *46*, 2377–2380.
- (55) Lim, F. Y.; Hou, Y.; Chen, Y.; Oh, J.-H.; Lee, I.; Bugni, T. S.; Keller, N. P. *Appl. Environ. Microbiol.* **2012**, *78*, 4117–4125.
- (56) Kikuchi, H.; Isobe, M.; Kurata, S.; Katou, Y.; Oshima, Y. *Tetrahedron* **2012**, *68*, 6218–6223.
- (57) Kurobane, I.; Vining, L. C.; McInnes, A. G. *J. Antibiot.* **1979**, *32*, 1256–1266.
- (58) Bok, J. W.; Chiang, Y.-M.; Szewczyk, E.; Reyes-Dominguez, Y.; Davidson, A. D.; Sanchez, J. F.; Lo, H.-C.; Watanabe, K.; Strauss, J.; Oakley, B. R.; Wang, C. C. C.; Keller, N. P. *Nat. Chem. Biol.* **2009**, *5*, 462–464.
- (59) Chiang, Y. M.; Szewczyk, E.; Davidson, A. D.; Entwistle, R.; Keller, N. P.; Wang, C. C.; Oakley, B. R. *Appl. Environ. Microbiol.* **2010**, *76*, 2067–2074.
- (60) Lu, P.; Zhang, A.; Dennis, L. M.; Dahl-Roshak, A. M.; Xia, Y. Q.; Arison, B.; An, Z.; Tkacz, J. S. *Mol. Genet. Genomics* **2005**, *273*, 207–216.
- (61) Lin, J.; Liu, S.; Sun, B.; Niu, S.; Li, E.; Liu, X.; Che, Y. *J. Nat. Prod.* **2010**, *73*, 905–910.
- (62) Sanchez, J. F.; Entwistle, R.; Hung, J.-H.; Yaegashi, J.; Jain, S.; Chiang, Y.-M.; Wang, C. C. C.; Oakley, B. R. *J. Am. Chem. Soc.* **2011**, *133*, 4010–4017.
- (63) Breinholt, J.; Demuth, H.; Lange, L.; Kjaer, A.; Pedersen, C. J. *Antibiot.* **1993**, *46*, 1013–1015.
- (64) Napolitano, J. G.; Gavin, J. A.; Garcia, C.; Norte, M.; Fernandez, J. J.; Daranas, A. H. *Chem.—Eur. J.* **2011**, *17*, 6338–6347.
- (65) Zhang, W.; Krohn, K.; Zia, U.; Flörke, U.; Pescitelli, G.; Di Bari, L.; Antus, S.; Kurtán, T.; Rheinheimer, J.; Draeger, S.; Schulz, B. *Chem.—Eur. J.* **2008**, *14*, 4913–4923.
- (66) Rönnsberg, D.; Debbab, A.; Mándi, A.; Wray, V.; Dai, H.; Kurtán, T.; Proksch, P.; Aly, A. H. *Tetrahedron Lett.* **2013**, *54*, 3256–3259.
- (67) Aly, A. H.; Edrada-Ebel, R.; Indriani, I. D.; Wray, V.; Müller, W. E.; Totzke, F.; Zirrgiebel, U.; Schächtele, C.; Kubbutat, M. H.; Lin, W. H.; Proksch, P.; Ebel, R. *J. Nat. Prod.* **2008**, *71*, 972–980.
- (68) Kjer, J.; Debbab, A.; Aly, A. H.; Proksch, P. *Nat. Protoc.* **2010**, *5*, 479–490.
- (69) Carmichael, J.; DeGraff, W. G.; Gazdar, A. F.; Minna, J. D.; Mitchell, J. B. *Cancer Res.* **1987**, *47*, 936–942.
- (70) Ashour, M.; Edrada, R. A.; Ebel, R.; Wray, V.; Wätjen, W.; Padmakumar, K.; Müller, W. E. G.; Lin, W. H.; Proksch, P. *J. Nat. Prod.* **2006**, *69*, 1547–1553.
- (71) Mueller, H.; Kassack, M. U.; Wiese, M. *J. Biomol. Screening* **2004**, *9*, 506–515.
- (72) Gosepath, E. M.; Eckstein, N.; Hamacher, A.; Servan, K.; von Jonquieres, G.; Lage, H.; Györfy, B.; Royer, H. D.; Kassack, M. U. *Int. J. Cancer* **2008**, *123*, 2013–2019.
- (73) Eckstein, N.; Servan, K.; Girard, L.; Cai, D.; von Jonquieres, G.; Jaehde, U.; Kassack, M. U.; Gazdar, A. F.; Minna, J. D.; Royer, H.-D. *J. Biol. Chem.* **2008**, *283*, 739–750.
- (74) Apex2: Data Collection Program for the CCD Area-Detector System; Bruker Analytical X-ray Systems: Madison, WI, 1997–2011. SAINT: Data Reduction and Frame Integration Program for the CCD Area-Detector System; Bruker Analytical X-ray Systems: Madison, WI, 1997–2011.
- (75) Sheldrick, G. SADABS: Program for Area-Detector Absorption Correction; University of Göttingen: Göttingen, Germany, 1996.
- (76) Sheldrick, G. *Acta Crystallogr., Sect. A* **2008**, *64*, 112–122.
- (77) Spek, A. L. PLATON: A Multipurpose Crystallographic Tool; Utrecht University: Utrecht, The Netherlands, 2008.
- (78) Farrugia, L. J. PLATON for Windows, version 40608; University of Glasgow: Glasgow, U.K., 2008.
- (79) Spek, A. J. *Appl. Crystallogr.* **2003**, *36*, 7–13.
- (80) Spek, A. *Acta Crystallogr., Sect. D* **2009**, *65*, 148–155.
- (81) Brandenburg, K. Diamond: Crystal and Molecular Structure Visualization Software, version 3.2; Crystal Impact: Bonn, Germany, 2009.
- (82) MacroModel; Schrödinger LLC: New York, 2012; <http://www.schrodinger.com/productpage/14/11/>
- (83) Frisch, M. J.; Trucks, G. W.; Schlegel, H. B.; Scuseria, G. E.; Robb, M. A.; Cheeseman, J. R.; Scalmani, G.; Barone, V.; Mennucci, B.; Petersson, G. A.; Nakatsuji, H.; Caricato, M.; Li, X.; Hratchian, H. P.; Izmaylov, A. F.; Bloino, J.; Zheng, G.; Sonnenberg, J. L.; Hada, M.; Ehara, M.; Toyota, K.; Fukuda, R.; Hasegawa, J.; Ishida, M.; Nakajima, T.; Honda, Y.; Kitao, O.; Nakai, H.; Vreven, T.; Montgomery, J. A., Jr.; Peralta, J. E.; Ogliaro, F.; Bearpark, M.; Heyd, J. J.; Brothers, E.; Kudin, K. N.; Staroverov, V. N.; Kobayashi, R.; Normand, J.; Raghavachari, K.; Rendell, A.; Burant, J. C.; Iyengar, S. S.; Tomasi, J.; Cossi, M.; Rega, N.; Millam, J. M.; Klene, M.; Knox, J. E.; Cross, J. B.; Bakken, V.; Adamo, C.; Jaramillo, J.; Gomperts, R.; Stratmann, R. E.; Yazyev, O.; Austin, A. J.; Cammi, R.; Pomelli, C.; Ochterski, J. W.; Martin, R. L.; Morokuma, K.; Zakrzewski, V. G.; Voth, G. A.; Salvador, P.; Dannenberg, J. J.; Dapprich, S.; Daniels, A. D.; Farkas, Ö.; Foresman, J. B.; Ortiz, J. V.; Cioslowski, J.; Fox, D. J. *Gaussian 09*, revision B.01; Gaussian, Inc.: Wallingford, CT, 2010.
- (84) Stephens, P. J.; Harada, N. *Chirality* **2010**, *22*, 229–233.
- (85) Varetto, U. MOLEKEL, version 5.4; Swiss National Supercomputing Centre: Manno, Switzerland, 2009.